

# 1 Quantifying the seasonal variations and regional transport of PM<sub>2.5</sub> 2 in the Yangtze River Delta region, China: Characteristics, sources, 3 and health risks

4 Yangzhihao Zhan<sup>a</sup>, Min Xie<sup>a,b</sup>, Wei Zhao<sup>c</sup>, Tijian Wang<sup>a</sup>, Da Gao<sup>d</sup>, Pulong Chen<sup>e</sup>, Jun Tian<sup>f</sup>, Kuanguang  
5 Zhu<sup>g</sup>, Shu Li<sup>a</sup>, Bingliang Zhuang<sup>a</sup>, Mengmeng Li<sup>a</sup>, Yi Luo<sup>a</sup>, Runqi Zhao<sup>a</sup>

6 <sup>a</sup> School of Atmospheric Sciences, Nanjing University, Nanjing 210023, China

7 <sup>b</sup> School of Environment, Nanjing Normal University, Nanjing 210023, China

8 <sup>c</sup> Nanjing Institute of Environmental Sciences, Ministry of Ecology and Environment of the People's Republic of China,  
9 Nanjing 210023, China

10 <sup>d</sup> State Key Joint Laboratory of Environment Simulation and Pollution Control, School of Environment, Tsinghua University,  
11 Beijing 100084, China

12 <sup>e</sup> Net Zero Era (Jiangsu) Environmental Technology Co., Nanjing 210023, China

13 <sup>f</sup> Academy of Environmental Planning and Design. Co.,Ltd., Nanjing University, Nanjing 210023, China

14 <sup>g</sup> Hubei Provincial Academy of Eco-Environmental Sciences, Wuhan 430073, China

15 *Correspondence to:* Min Xie (minxie@nju.edu.cn), Wei Zhao (zhaowei@nies.org)

16 **Abstract.** Given the increasing complexity of the chemical composition of PM<sub>2.5</sub>, identifying and quantitatively assessing  
17 the contributions of pollution sources has played an important role in formulating policies to control particle pollution. This  
18 study provides a comprehensive assessment between PM<sub>2.5</sub> chemical characteristics, sources, and health risks based on  
19 sampling data conducted over one year (March 2018 to February 2019) in Nanjing. Results show that PM<sub>2.5</sub> exhibits a  
20 distinct variation across different seasons, which is primarily driven by emissions, meteorological conditions, and chemical  
21 conversion of gaseous pollutants. First, the chemical mass reconstruction shows that secondary inorganic aerosols (SIA,  
22 62.5 %) and carbonaceous aerosols (21.3%) contributed most to the PM<sub>2.5</sub> mass. The increasing oxidation rates of SO<sub>2</sub> and  
23 NO<sub>2</sub> from summer to winter indicate that the secondary transformation of gaseous pollutants is strongly positively correlated  
24 with relative humidity. Second, the positive matrix factorization (PMF) method shows that identified PM<sub>2.5</sub> sources include  
25 secondary inorganic aerosol sources (SIS, 42.5%), coal combustion (CC, 22.4%), industry source (IS, 17.3%), vehicle  
26 emission (VE, 10.7%), fugitive dust (FD, 5.8%) and other sources (1.3%). The Hybrid Single Particle Lagrangian Integrated  
27 Trajectory (HYSPLIT) model and the concentration-weighted trajectory (CWT) analysis are used to further explore different  
28 spatial distributions and regional transport of sources. The concentrations (10-11 μg·m<sup>-3</sup>) of SIS and CC distribute in  
29 Nanjing and central China in winter. The concentrations (8-10 μg·m<sup>-3</sup>) of IS and VE are potentially located north of Jiangsu,  
30 Anhui, and Jiangxi. Finally, the health risk assessment indicates that the carcinogenic and non-carcinogenic risks of toxic  
31 elements (Cr, As, Ni, Mn, V, and Pb) mainly come from IS, VE, and CC, which are within the tolerance or acceptable level.  
32 Although the main source of pollution in Nanjing is SIS at present, we should pay more attention to the health burden of  
33 vehicle emissions, coal combustion, and industrial processes.

## 35 1. Introduction

36 PM<sub>2.5</sub> is particulate matter with an aerodynamic equivalent diameter less than or equal to 2.5 μm, and one of the most  
37 important air pollutants, which can affect air quality (Sharma et al., 2020), atmospheric visibility (Tseng et al., 2019) and  
38 ecosystems (Li et al., 2021). PM<sub>2.5</sub> can directly enter the human body through the respiratory system and lead to increased  
39 health risks (Kumar et al., 2019; Sulaymon et al., 2021). PM<sub>2.5</sub> concentrations in the United States and Europe have begun to  
40 decrease since the 1980s, and those in Japan gradually decreased after 2012 (Zhang et al., 2020). In China, the annual  
41 average concentration of PM<sub>2.5</sub> has decreased by 50% with the implementation of the Air Pollution Prevention and Control  
42 Action Plan (APPCAP) in 2013. However, annual PM<sub>2.5</sub> concentrations in most cities are greater than 10 μg·m<sup>-3</sup>, the air  
43 quality guideline of the World Health Organization (Song et al., 2017; Zeng et al., 2019; Cheng et al., 2021), and the number  
44 of deaths caused by PM<sub>2.5</sub> exceeds one million per year (Zhu et al., 2020). It indicates that a comprehensive assessment  
45 between PM<sub>2.5</sub> chemical characteristics, sources, and health risks is significant for pollution control measures in the key  
46 regions of China.

47 Understanding the chemical composition of PM<sub>2.5</sub> is important for formulating control strategies. Sulfate, nitrate, and  
48 ammonium (SNA) are the major secondary inorganic aerosols, whose chemical conversion occurs in homogeneous and  
49 heterogeneous reactions (Fan et al., 2020; Chow et al., 2022). Variations in the form of SO<sub>4</sub><sup>2-</sup> and NH<sub>3</sub> lead to variations in  
50 the acid-base balance of aerosols (Roper et al., 2019). Organic carbon (OC) comprises thousands of organic compounds.  
51 Elemental carbon (EC) is stable and mainly derived from primary sources of combustion products (Wu et al., 2020; Zhang et  
52 al., 2022). Both NO<sub>3</sub><sup>-</sup>/SO<sub>4</sub><sup>2-</sup> and OC/EC ratios can be reasonably used to evaluate the contribution of mobile and stationary  
53 sources to PM<sub>2.5</sub> in the atmosphere (Zhan et al., 2021). To identify the sources of PM<sub>2.5</sub>, receptor modelings have been  
54 developed, which include positive matrix factorization (PMF), chemical mass balance (CMB), and principal component  
55 analysis (PCA) (Zong et al., 2016; Lv et al., 2020). Recently, the combination of the PMF model and trajectory modeling has  
56 proven to be powerful to identify source regions and quantify chemical compositions for a receptor site (Zheng et al., 2019).  
57 Air exposure models have been widely used to compare the health outcomes of people exposed to different levels of air  
58 pollution (Thurston et al., 2016; Conibear et al., 2018). Long-term exposure to PM<sub>2.5</sub> is particularly significant for  
59 cardiovascular disease mortality (Hayes et al., 2020). Trace metals (Cr, Ni, Mn, V, and Pb) are a minor component of PM<sub>2.5</sub>  
60 in qualitative terms, but the health risk of toxic elements through inhalation of PM<sub>2.5</sub> exceeds acceptable levels (Jiang et al.,  
61 2018; Jeong et al., 2019; Xie et al., 2020). Health risk assessments have been widely used to assess further the non-  
62 carcinogenic and carcinogenic health risks of toxic elements in PM<sub>2.5</sub> (Behrooz et al., 2021; Fang et al., 2021; Li et al., 2022).

63 Chemical characteristics of PM<sub>2.5</sub> have been widely investigated in the Beijing-Tianjin-Hebei (BTH), the Yangtze River  
64 Delta (YRD), and the Pearl River Delta (PRD) during the last decade (Huang et al., 2017; Liu et al., 2017; Li et al., 2020). In  
65 the megacity of China, the occurrence of haze may be exacerbated by interactions between aerosols and meteorological  
66 conditions and regional transport (Zeng et al., 2019; Fan et al., 2020; Wang et al., 2023). The YRD region is China's  
67 scientific research base and comprehensive transportation hub. The annual PM<sub>2.5</sub> concentration in the YRD has been reduced

68 by 45.6% from 2016 to 2018. However, as a mega-city in the YRD, the PM<sub>2.5</sub> in Nanjing still exceeds the National Ambient  
69 Air Quality Standard (35 µg·m<sup>-3</sup> as an annual average) by more than 38 % (Nie et al., 2018). Source apportionment studies  
70 mainly focus on the relative importance of local emission and regional transportation on PM<sub>2.5</sub> at a specific site using the  
71 PMF model and the backward trajectory analysis (Zheng et al., 2019; Yan et al., 2021; Lv et al., 2022). Some studies  
72 involved the health risks of toxic elements in PM<sub>2.5</sub> (Zhang et al., 2019; Fang et al., 2021), and only a few studies discussed  
73 the classification of toxic elements according to PMF results (Wang et al., 2019; Wang et al., 2020). However, there were  
74 two shortcomings in previous studies: (1) Given the uneven geographical distribution of observation sites and difficulties in  
75 data collection, most studies were based on short-term data comparisons and lacked systematic comparisons of the  
76 distinctive seasonality, regional transport, and meteorological effects of various elements and sources. (2) A comprehensive  
77 assessment of the health risks of toxic elements in each source of PM<sub>2.5</sub> was still scarce, which limited the implementation of  
78 long-term pollution control measures in megacities.

79 In this work, we provide high-quality composition data for PM<sub>2.5</sub> in the typical YRD city, including their chemical  
80 characteristics and diurnal variations. Besides, the measured PM<sub>2.5</sub> in its entirety is successfully apportioned to various  
81 contributing sources by PMF and CWT methods. Finally, potential risks associated with exposure to airborne toxic elements  
82 are identified based on the health risk assessment. The results can systematically assess the relationship between chemical  
83 characteristics, sources, and health risks of PM<sub>2.5</sub>, and serve to guide PM<sub>2.5</sub> control measures for other megacities.

84

## 85 **2. Data and Methodology**

### 86 **2.1 Chemical component sampling, air quality and meteorological data**

87 Hourly concentrations of particulate matter (PM) components from December 2018 to February 2019 in Nanjing were  
88 used in this study. PM<sub>2.5</sub> samples were collected on the rooftop of the School of Atmospheric Sciences, Xianlin Campus,  
89 Nanjing University (32.12 °N, 118.96 °E). The elemental carbon (EC), organic carbon (OC), 30 trace elements, and 8  
90 soluble components in aerosols were quantified in each PM<sub>2.5</sub> sample.

91 EC and OC samples were analyzed by the online carbon fraction Monitor (EA-32, Everisetech Co., Beijing). Taking  
92 advantage of the fact that EC was more difficult to be volatilized than OC, the instrument separated OC and EC by step  
93 heating, catalyzed sequentially, and then determined by the non-dispersive infrared method.

94 30 trace elements included Si, Al, As, Ca, K, Co, Mo, Ag, Sc, Tl, Pd, Br, Te, Ga, Cs, Pb, Se, Hg, Cr, Cd, Zn, Cu, Ni, Fe,  
95 Mn, Ti, Sb, Sn, and V. The components of trace elements were collected by the atmospheric heavy metal Monitor (AMS-100,  
96 Fpigroup Co., Hangzhou). We used a particle cutting head to collect particles with an aerodynamic equivalent diameter of  
97 less than 100/10/2.5 µm in the ambient air, used organic microporous filter membranes to enrich the collected particles, used  
98 the principle of β-ray absorption to detect the concentration of particles enriched on the filter membranes and used the  
99 principle of X-ray Fluorescence to detect the concentration of more than 30 types of trace elements in the particles (Wang et  
100 al., 2020).

101 8 soluble components included  $\text{Na}^+$ ,  $\text{K}^+$ ,  $\text{Mg}^{2+}$ ,  $\text{Ca}^{2+}$ ,  $\text{Cl}^-$ ,  $\text{NO}_3^-$ ,  $\text{SO}_4^{2-}$ , and  $\text{NH}_4^+$ . The soluble components sampling  
102 instrument was the In-situ Gas and Aerosol Compositions Monitor (IGAC, Fortelice International Co., Taiwan). It consisted  
103 of the wet concentric circular tube, the gas gel processor, and the ion chromatograph. The sampling inlet was about 20 m  
104 above the ground and the flow rate was  $16.67 \text{ L}\cdot\text{min}^{-1}$ . The collected liquid samples were filtered by defoaming and then  
105 injected into the ion chromatography analyzers to analyze the ion components from the gases and the aerosols. The detection  
106 limits were below  $0.12 \mu\text{g}\cdot\text{m}^{-3}$  and the collection efficiency was higher than 90% (Zhan et al., 2021).

107 Air pollutants, including  $\text{PM}_{2.5}$ ,  $\text{PM}_{10}$ ,  $\text{O}_3$ ,  $\text{NO}_2$ ,  $\text{SO}_2$ , and  $\text{CO}$ , were monitored by the National Environmental  
108 Monitoring Center (NEMC) of China. The nationwide observation network began operating in 74 major cities in 2013, and it  
109 included 1597 nonrural sites covering 454 cities by 2017 (Gao et al., 2021). The monitoring Xianlin Station ( $32.10^\circ\text{N}$ ,  
110  $118.93^\circ\text{E}$ ) collected air pollutant data and automatically measured hourly air pollutants. These data were issued hourly on  
111 the national urban air quality real-time publishing platform (<https://air.cnemc.cn:18007/>, last access: 7 April 2023).  
112 Meteorological parameters included air pressure, air temperature, relative humidity, wind speed, and boundary layer height.  
113 We collected hourly data from the National Climatic Data Center (NCDC) of the University of Wyoming website  
114 (<http://weather.uwyo.edu/surface/>, last access: 7 April 2023). Regarding boundary layer height, daily sounding vertical  
115 profiles were extracted from the national benchmark climate Nanjing station 58238 ( $32.00^\circ\text{N}$ ,  $118.48^\circ\text{E}$ ) and were also  
116 acquired from this website. The quality assurance and quality control (QA/QC) procedures were used at each site according  
117 to the method of Xie et al. (2016) and Gao et al. (2021).  $\text{PM}_{2.5}$  component data were collected hourly, and the study was  
118 based on high-time resolution data. We measured 10% of all samples as parallel sampling and the pass rate was over 95%.  
119 We defined the missing sampling of atmospheric pollutant data as -999 to facilitate PMF processing. The chemical mass  
120 reconstruction method was used to correct potential measurement errors, which was described in detail in Section 2.2. The  
121 QA/QC procedures have passed the artificial random inspection of extreme value and time consistency.

## 122 **2.2 Mass and chemical composition determination for $\text{PM}_{2.5}$**

123 Due to the limitation in sampling location and equipment, the sum of measured species was often lower than the  
124 gravimetric mass. Chemical mass reconstruction (CMR) attempted to achieve closure between the gravitational mass and the  
125 sum of components and correct potential measurement errors. In this study, the reconstructed result and the gravimetric  
126 result exhibited a significant correlation, with a mean  $R^2$  of 0.93, indicating that the chemical reconstruction method had  
127 strong reliability. Following the work of Xu et al. (2021), eight categories of chemical components in chemically  
128 reconstructed  $\text{PM}_{2.5}$  can be expressed as follows:

$$129 \quad PM_{2.5} = OM + EC + MD + TM + SO_4^{2-} + NO_3^- + NH_4^+ + Cl^- \quad (1)$$

130 where OM refers to the organic matter. The OC to OM conversion coefficient at urban sites is 1.6 (Brokamp et al., 2017).  
131 The calculation of mineral dust (MD) is based on crustal element oxides (Yan et al., 2020):

$$132 \quad MD = 2.14 \times Si + 1.67 \times Ti + 1.89 \times Al + 1.40 \times Ca + 1.58 \times Mn + 1.43 \times Fe + 1.21 \times K + 1.67 \times Mg \quad (2)$$

133 where  $S_i$  is estimated as multiplying  $Al$  in crustal material by a converting factor (3.14) (Zheng et al., 2019). Trace metals  
 134 (TM) represent the sum of 30 different types of heavy metals:

$$135 \quad TM = As + Co + Mo + Ag + Sc + Tl + Pd + Br + Te + Ga + Cs + Pb \\ + Se + Hg + Cr + Cd + Zn + Cu + Ni + Sb + Sn + V + Ba \quad (3)$$

### 136 2.3 Identification of source by the positive matrix factorization (PMF) model

137 The positive matrix factorization (PMF) was developed by the Environmental Protection Agency (EPA) and has been  
 138 widely adopted to classify  $PM_{2.5}$  into different factors (Zong et al., 2016). The US EPA PMF version 5.0 was referred to in  
 139 this study. The basic principle of the PMF model was to calculate the weight error of each chemical component in the  
 140 particulate matter and then determined its main pollution source and contribution rate by the least square method (Paatero  
 141 and Tapper, 1994). The equation of the PMF model can be expressed as follow:

$$142 \quad X_{ij} = \sum_{k=1}^p g_{ik} f_{kj} + e_{ij} \quad (4)$$

143 where  $X_{ij}$  is the concentration of the  $ij$ th sample;  $g_{ik}$  represents the contribution of the  $ik$ th sample;  $f_{kj}$  represents the  
 144 mass fraction of the  $jk$ th and  $e_{ij}$  is the residual between the measured mass concentration of the  $ij$ th sample and its analytical  
 145 value. The purpose of the PMF model is to find the minimum Q value with the concentration file and uncertainty file ( $u_{ij}$ )  
 146 introduced into the model. The objective function Q is defined as follows:

$$147 \quad Q_{ij} = \sum_{i=1}^n \sum_{j=1}^m \left[ \frac{X_{ij} - \sum_{k=1}^p g_{ik} f_{kj}}{u_{ij}} \right]^2 \quad (5)$$

148 where Q is the sum of all sample residuals and their uncertainties  $u$ . In this study, the fitting species included 41 types of  
 149 chemical species of  $PM_{2.5}$  that were selected and validated to ensure that the value of the objective function Q was  
 150 minimized.

$$151 \quad Unc = \frac{5}{6} \times MDL \quad (6)$$

$$152 \quad Unc = \sqrt{(Error\ Fraction \times concentration)^2 + (0.5 \times MDL)^2} \quad (7)$$

153 where Unc is the uncertainty. MDL is the method detection limit. If the concentration is less than or equal to the MDL  
 154 provided, Unc is calculated using a fixed fraction of the MDL (Taylor et al., 2020). If the concentration is greater than the  
 155 MDL, the calculation is based on the concentration fraction and MDL.

156 First, we excluded more than 50% of the dataset for species below the method detection limit (MDL) and retained 23  
157 species that were significantly correlated with PM<sub>2.5</sub>. Second, we calculated the uncertainty (Unc) for each species based on  
158 the concentration fraction and MDL (Taylor et al., 2020). Third, different numbers of factors were tested with random seeds  
159 in 20 iterations of each run. When the number of factors was set to six, the fitting degree of the model calculation results was  
160 the highest, with a correlation coefficient of 0.93, and the species almost showed a normal curve. Finally, the bootstrap (BS)  
161 and displacement (DISP), and BS-DISP diagnostic analysis were also used to evaluate the rationality of the apportioned  
162 factor profiles and contributions. BS is used to detect and estimate the disproportionate effects of a small set of observations  
163 on the solution and also, to a lesser extent, the effects of rotational ambiguity. The value of the F-peak strength was ensured  
164 to be 0.5 to eliminate the rotation ambiguity. The mapping for each factor in this study was more than 80% from the BS run,  
165 indicating the six-factor solution was appropriate.

#### 166 **2.4 Source apportionment by backward trajectory calculation and CWT analysis**

167 The Hybrid Single Particle Lagrangian Integrated Trajectory (HYSPLIT) model was developed by the National  
168 Oceanic and Atmospheric Administration (NOAA) and the Bureau of Meteorology Australia to simulate and analyze the  
169 movement, deposition, and diffusion of airflow. The reanalysis data with a spatial resolution of one degree and a temporal  
170 resolution of 6 h (00:00, 06:00, 12:00, and 18:00 UTC) were obtained from the Global Data Assimilation System (GDAS)  
171 (<https://rda.ucar.edu/datasets/>, last access: 7 April 2023). To locate the potential source areas for the corresponding  
172 components, we used the HYSPLIT model to analyze the backward trajectory of airflow from March 2018 to February 2019.  
173 48-hour backward trajectories terminated at a height of 100 m above ground level were calculated at the starting point  
174 (32.07 °N, 118.78 °E). Due to the high uncertainty of a single backward trajectory, we drew multiple trajectories and  
175 performed cluster analysis. The cluster analysis was a multivariate statistical technique using the Angle Distance algorithm,  
176 which could quantify the relationship among the pollution concentrations in each source area (Shu et al., 2017).

177 The concentration-weighted trajectory (CWT) analysis was further used to determine the relative contribution of  
178 different areas. The CWT analysis was conducted by the TrajStat software, which was a GIS (geographic information system)  
179 application that enabled the user to visualize and analyze the spatial and meteorological data with multiple data formats  
180 (Feng et al., 2021). In this study, the meteorological data used for the HYSPLIT model and the CWT method remained the  
181 same. The CWT method divided the research area into small equal grids, set a standard value for the research object, and  
182 defined the trajectory exceeding the standard value as the pollution trajectory. According to the criteria of the Chinese  
183 National Ambient Air Quality Standards (NAAQS), the standard value of the PM<sub>2.5</sub> concentrations was 75 µg·m<sup>-3</sup> in this  
184 study. The spatial resolution was 0.5×0.5 (Liu et al., 2018). The CWT method reflected the pollution degree of different  
185 trajectories by calculating the weight concentration of the airflow trajectory in potential source areas:

$$186 \quad C_{ij} = \frac{1}{\sum_{i=1}^M \tau_{ijl}} \sum_{l=1}^M C_l \tau_{ijl} \quad (8)$$

187 where  $C_{ij}$  is the average weight concentration of grid  $ij$ ,  $C_l$  is the pollutant concentration based on trajectory  $l$  that passes  
 188 through grid  $ij$ , and  $\tau_{ij}$  is the residence time of trajectory  $l$  in grid  $ij$ . Similarly, to reduce the uncertainty caused by the  
 189 smaller  $n_{ij}$ , the CWT value is multiplied by the weight function as well (Wong et al., 2022):

$$190 \quad W_{ij} = \begin{cases} 1.00 & (80 < n_{ij}) \\ 0.72 & (20 < n_{ij} \leq 80) \\ 0.42 & (10 < n_{ij} \leq 20) \\ 0.05 & (n_{ij} \leq 100) \end{cases} \quad (9)$$

191 where  $n_{ij}$  is the number of trajectories that pass through the  $ij^{\text{th}}$  cell.  $W_{ij}$  is an empirical weight function to reduce the undue  
 192 influence of small  $n_{ij}$  on the CWT values (Fan et al., 2019). In this study, the CWT value of each identified source derived  
 193 from the PMF model was calculated.

## 194 2.5 Health risk assessment

195 The human health risk from heavy metals in PM<sub>2.5</sub> may occur through exposure to ambient air (Zhang et al., 2019).  
 196 Based on the PMF analysis, we selected six toxic elements (Cr, As, Ni, Mn, V, and Pb) for the exposure risk assessment. Cr,  
 197 Ni and As have both carcinogenic and non-carcinogenic effects, Mn and V mainly have non-carcinogenic effects, and Pb  
 198 mainly produces a carcinogenic effect (Jiang et al., 2018). The non-carcinogenic and carcinogenic risks from the toxic  
 199 species of PM<sub>2.5</sub> were evaluated by the hazard quotient (HQ) and lifetime carcinogenic risk (LCR), respectively. The US  
 200 EPA human health risk assessment models were used to conduct carcinogenic and non-carcinogenic risk assessments (Khan  
 201 et al., 2016):

$$202 \quad EC_{inh} = \frac{GA \times ET \times EF \times ED}{AT} \quad (10)$$

$$203 \quad HQ = \frac{EC_{inh}}{RfC_i \times 1000 \mu\text{g} \cdot \text{mg}^{-1}} \quad (11)$$

$$204 \quad LCR = IUR \times EC_{inh} \quad (12)$$

205 where  $EC_{inh}$  is the average daily exposure concentration of toxic elements inhaled through respiration.  $GA$  is the  
 206 concentration of toxic elements in each source composition.  $ET$  is the exposure time, 24 h·d<sup>-1</sup>;  $EF$  is the exposure frequency,  
 207 365 d·yr<sup>-1</sup>;  $ED$  is the exposure duration, 30 yr; and  $AT$  is the average exposure time, calculated by  $ED \text{ yr} \times 365 \text{ d} \cdot \text{yr}^{-1} \times 24$   
 208 h·d<sup>-1</sup> for non-carcinogens and  $70 \text{ yr} \times 365 \text{ d} \cdot \text{yr}^{-1} \times 24 \text{ h} \cdot \text{d}^{-1}$  for carcinogens.  $RfC_i$  is the inhalation reference concentration  
 209 (mg·m<sup>-3</sup>).  $IUR$  is the inhalation unit risk((μg·m<sup>-3</sup>)<sup>-1</sup>). HQ greater than 1 indicated a non-carcinogenic risk to human health.

210 For carcinogenic risk, LCR < 10<sup>-6</sup> means no cancer risk, LCR between 10<sup>-6</sup> and 10<sup>-4</sup> is acceptable or tolerable, and LCR > 10<sup>-4</sup> is intolerable. The exposure parameters were shown in Table 1 (Jiang et al., 2018; Zhang et al., 2019).

212

213 **Table 1. Exposure parameters of toxic elements through inhalation route in health risk assessments.**

Toxic elements	RfCi ( $\mu\text{g}\cdot\text{m}^{-3}$ ) <sup>-1</sup>	IUR ( $\text{mg}\cdot\text{m}^{-3}$ )
Cr	1.0×10 <sup>-4</sup>	1.2×10 <sup>-2</sup>
As	1.5×10 <sup>-5</sup>	4.3×10 <sup>-3</sup>
Ni	1.4×10 <sup>-5</sup>	2.4×10 <sup>-4</sup>
Mn	5.0×10 <sup>-5</sup>	—
V	1.0×10 <sup>-4</sup>	—
Pb	—	1.2×10 <sup>-5</sup>

214

### 215 **3. Results and discussions**

#### 216 **3.1 Chemical components, meteorological parameters and diurnal variations**

217 Table 2 shows the seasonal average of chemical components and meteorological parameters from March 2018 to  
218 February 2019. In this study, March to May 2018 is defined as spring, June to August 2018 is defined as summer, September  
219 to November 2018 is defined as fall, and December 2018 to February 2019 is defined as winter. The daily average  
220 concentration of PM<sub>2.5</sub> ranged from 6.7 to 234.0  $\mu\text{g}\cdot\text{m}^{-3}$ , with an annual average of 68.7  $\mu\text{g}\cdot\text{m}^{-3}$ . The order of average  
221 concentrations of PM<sub>2.5</sub> in each season was winter (113.9  $\mu\text{g}\cdot\text{m}^{-3}$ ) > spring (99.1  $\mu\text{g}\cdot\text{m}^{-3}$ ) > autumn (38.9  $\mu\text{g}\cdot\text{m}^{-3}$ ) > summer  
222 (23.7  $\mu\text{g}\cdot\text{m}^{-3}$ ). Seasonal variations of PM<sub>2.5</sub> were closely related to emission and meteorological conditions. In spring, the  
223 wind speed (WS) was higher (3.5  $\text{m}\cdot\text{s}^{-1}$ ) than those in other seasons. Pearson correlation showed that PM<sub>2.5</sub> concentrations  
224 were significantly ( $p<0.01$ ) correlated to WS ( $r=-0.36$ ) in spring. In summer, high boundary layer height (BLH) (520.4m)  
225 significantly reduced PM<sub>2.5</sub> concentrations. In autumn and winter, PM<sub>2.5</sub> showed significant correlations between  
226 temperature ( $r=-0.53$ ), relative humidity ( $r=0.62$ ) and BLH ( $r=-0.43$ ). Biomass burning and industrial emissions are  
227 important sources of aerosols in the urban atmosphere and contribute 7-27% to PM<sub>2.5</sub> mass in applicable cities (Tao et al.,  
228 2017; Andreae et al., 2019). Coal consumption and population density have a significantly positive effect on PM<sub>2.5</sub>  
229 concentration (Zhou et al., 2018; Chow et al., 2022). The highest level of PM<sub>2.5</sub> in winter was due to coal consumption,  
230 lower temperatures (4.9°C), higher humidity (79.6%), and lower BLH (419.7m) than in summer.

231 The seasonal variation of anthropogenic emissions also considerably affected PM<sub>2.5</sub> concentrations. The order of the  
232 major components in PM<sub>2.5</sub> was NO<sub>3</sub><sup>-</sup> (20-31%) > SO<sub>4</sub><sup>2-</sup> (16-27%) > NH<sub>4</sub><sup>+</sup> (11-19%) > mineral dust (8-14%) > OM (6-  
233 14%) > EC (2-4%) > trace metals (2-3%) > Cl<sup>-</sup> (1-3%). Sulfate, nitrate, and ammonium (SNA) accounted for 60% of the  
234 total PM<sub>2.5</sub> and were closely related to the secondary transformation of gaseous precursors. The concentration ratio of NO<sub>3</sub><sup>-</sup>  
235 to SO<sub>4</sub><sup>2-</sup> (NO<sub>3</sub><sup>-</sup>/SO<sub>4</sub><sup>2-</sup>) was used to differentiate the relative importance of nitrogen (generally related to vehicle emissions)  
236 and sulfur (normally related to stationary sources) in the atmosphere (Liu et al., 2019). Over the past few years, the mass



237 ratio of  $\text{NO}_3^-/\text{SO}_4^{2-}$  was 2.13 in Ningbo, 1.89 in Hangzhou, and 1.21 in Beijing (Huang et al., 2017; Li et al., 2018). In this  
 238 study, the average ratios of  $\text{NO}_3^-/\text{SO}_4^{2-}$  were 1.81 in spring, 1.20 in summer, 2.34 in autumn, and 1.59 in winter, respectively,  
 239 indicating the enhanced secondary transformation of gaseous pollutants (e.g.  $\text{SO}_2$ ,  $\text{NO}_x$ , VOCs) during heavily polluted  
 240 periods (Liu et al., 2016; Liu et al., 2018). The oxidation rates of  $\text{SO}_2$  and  $\text{NO}_2$  need to be further investigated.  
 241 Carbonaceous aerosols (OM and EC) accounted for 12% and 14% of  $\text{PM}_{2.5}$  in spring and winter, respectively. The large  
 242 increase in the number of coal fires used for residential heating in winter may increase the abundance of carbon-containing  
 243 emissions, including OC, EC, and VOCs (Islam et al., 2020). Compared with 2015, the concentrations of OM and EC  
 244 decreased from 22.9% to 12.8% (Chen et al., 2017). This may be related to policies to control coal combustion and motor  
 245 vehicle emissions, considering similar meteorological conditions in the two periods (Tao et al., 2017; Jeong et al., 2019).

246

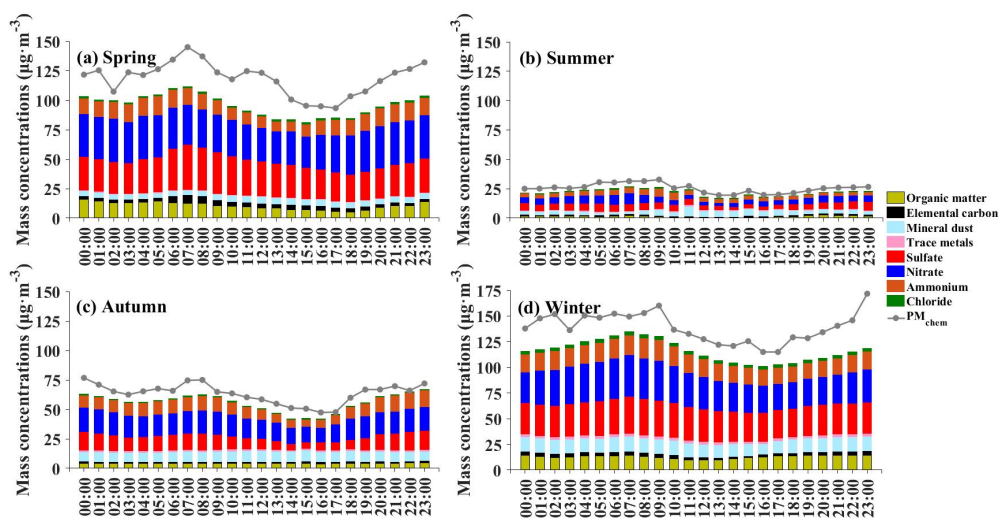
247 **Table 2. Seasonal average concentration of components of  $\text{PM}_{2.5}$ , in  $\mu\text{g}\cdot\text{m}^{-3}$  and % in brackets, and meteorological parameters. T,**  
 248 **RH, WS, and BLH represent air temperature, relative humidity, wind speed and boundary layer height, respectively.**

Components and meteorological parameters	Spring	Summer	Autumn	Winter
$\text{PM}_{2.5}$	$99.1 \pm 29.5$	$23.7 \pm 12.2$	$38.9 \pm 20.6$	$113.9 \pm 43.6$
$\text{SO}_4^{2-}$	$20.5 \pm 5.9$ (20.7)	$5.2 \pm 2.1$ (21.9)	$7.3 \pm 4.8$ (18.8)	$31.5 \pm 8.7$ (27.7)
$\text{NO}_3^-$	$16.9 \pm 11.4$ (17.1)	$5.3 \pm 1.2$ (22.4)	$9.8 \pm 3.3$ (25.2)	$27.2 \pm 17.5$ (23.9)
$\text{NH}_4^+$	$15.1 \pm 6.1$ (15.2)	$3.2 \pm 1.7$ (13.5)	$7.1 \pm 2.1$ (18.3)	$11.5 \pm 4.6$ (10.1)
OM	$11.7 \pm 6.1$ (11.8)	$1.6 \pm 0.7$ (6.8)	$4.1 \pm 1.1$ (10.5)	$11.0 \pm 5.8$ (9.7)
EC	$2.3 \pm 0.8$ (2.3)	$0.8 \pm 0.3$ (3.4)	$1.6 \pm 1.2$ (4.1)	$3.6 \pm 1.5$ (3.2)
Mineral dust	$13.2 \pm 4.5$ (13.3)	$2.3 \pm 0.8$ (9.7)	$2.7 \pm 1.0$ (6.9)	$8.7 \pm 2.7$ (7.6)
Trace metals	$2.7 \pm 1.5$ (2.7)	$0.5 \pm 0.1$ (2.1)	$0.5 \pm 0.2$ (1.3)	$1.6 \pm 0.9$ (1.4)
$\text{Cl}^-$	$2.7 \pm 0.9$ (2.7)	$1.6 \pm 0.6$ (6.8)	$0.8 \pm 0.2$ (2.1)	$1.7 \pm 0.4$ (1.5)
T ( $^{\circ}\text{C}$ )	$18.8 \pm 4.3$	$27.6 \pm 5.4$	$19.4 \pm 4.9$	$4.9 \pm 2.2$
RH (%)	$86.5 \pm 12.9$	$58.2 \pm 6.3$	$73.1 \pm 8.5$	$79.6 \pm 10.4$
WS ( $\text{m}\cdot\text{s}^{-1}$ )	$3.5 \pm 0.6$	$2.9 \pm 0.5$	$2.7 \pm 0.5$	$2.1 \pm 0.3$
BLH (m)	$469.7 \pm 40.9$	$520.4 \pm 58.9$	$443.6 \pm 32.4$	$419.7 \pm 23.5$

249

250 Figure 1 shows the diurnal variation of chemical components in  $\text{PM}_{2.5}$ . The seasonal differences were mainly reflected  
 251 in the variation in the timing of peak values. In spring (Fig. 1a), the highest and lowest  $\text{PM}_{2.5}$  concentrations were  $143.6$   
 252  $\mu\text{g}\cdot\text{m}^{-3}$  at 7:00 and  $94.8 \mu\text{g}\cdot\text{m}^{-3}$  at 14:00, respectively. The concentration of SNA had obvious diurnal variations. From 6:00  
 253 to 18:00, the average concentration of  $\text{NO}_3^-$  increased from  $17.6$  to  $21.8 \mu\text{g}\cdot\text{m}^{-3}$ , while the average concentration of  $\text{SO}_4^{2-}$   
 254 decreased from  $23.2$  to  $15.9 \mu\text{g}\cdot\text{m}^{-3}$ . In summer (Fig. 1b), the highest and lowest  $\text{PM}_{2.5}$  concentrations were  $23.5 \mu\text{g}\cdot\text{m}^{-3}$  at  
 255 9:00 and  $14.2 \mu\text{g}\cdot\text{m}^{-3}$  at 14:00, respectively. The maximum concentration difference of SNA between day and night was less

256 than  $10 \mu\text{g}\cdot\text{m}^{-3}$ , indicating the study area was in a relatively stable background field (Chen et al., 2018). In autumn (Fig. 1c),  
 257 the highest and lowest  $\text{PM}_{2.5}$  concentrations were  $77.1 \mu\text{g}\cdot\text{m}^{-3}$  at 8:00 and  $47.8 \mu\text{g}\cdot\text{m}^{-3}$  at 16:00, respectively. The  
 258 concentration of SNA increased at night and decreased during the day. The maximum concentration difference was more  
 259 than  $20 \mu\text{g}\cdot\text{m}^{-3}$ . In winter (Fig. 1d), from 18:00 to 23:00, the concentration of SNA increased from  $74.5 \mu\text{g}\cdot\text{m}^{-3}$  to  $108.7$   
 260  $\mu\text{g}\cdot\text{m}^{-3}$ , with increasing rates of  $8.5 \mu\text{g}\cdot\text{m}^{-3}\cdot\text{h}^{-1}$ . The height of the atmospheric boundary layer decreased early in the winter  
 261 afternoons (Chen et al., 2018). The values of  $\text{PM}_{2.5}$  in winter were higher at night due to the coal combustion and biomass  
 262 burning (BB) for residential heating (Zou et al., 2017). In summary, compared with the spring and winter,  $\text{PM}_{2.5}$  presented  
 263 similar and relatively flat diurnal patterns in both autumn and summer. Although the seasonal variations of mass  
 264 concentrations and aerosol compositions were substantially different, the concentrations of aerosol species showed similar  
 265 diurnal variation patterns during all the sampling days with higher values in the nighttime and early morning, suggesting that  
 266 the factors driving the diurnal variations were similar.  
 267



268  
 269 **Figure 1. Average diurnal variation of the concentrations of major chemical components of  $\text{PM}_{2.5}$  per each season.**  
 270

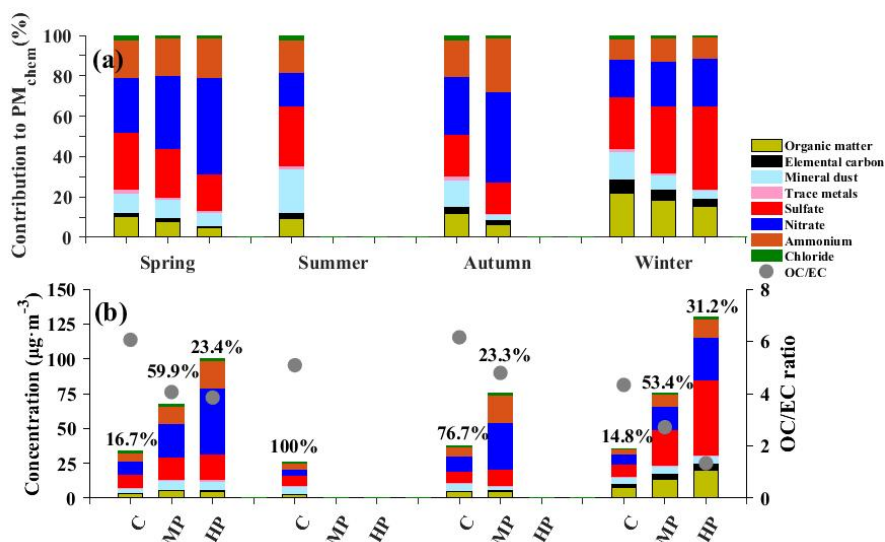
### 271 3.2 Variation of $\text{PM}_{2.5}$ chemical compositions at different pollution levels

272 Figure 2 presents the  $\text{PM}_{2.5}$  concentrations and components at different pollution levels. In this study, it was defined as  
 273 the clean day (C) when the daily average  $\text{PM}_{2.5}$  concentrations were less than  $35 \mu\text{g}\cdot\text{m}^{-3}$ , the moderate pollution day (MP)  
 274 when  $\text{PM}_{2.5}$  concentrations were more than  $35 \mu\text{g}\cdot\text{m}^{-3}$  and less than  $150 \mu\text{g}\cdot\text{m}^{-3}$ , and the heavy pollution day (HP) when  
 275  $\text{PM}_{2.5}$  concentrations were more than or equal to  $150 \mu\text{g}\cdot\text{m}^{-3}$ . As shown in Figure 2a, the annual average concentration of the  
 276 water-soluble inorganic ions (WSIIs) was  $41.9 \mu\text{g}\cdot\text{m}^{-3}$ , and accounted for 61.8% of  $\text{PM}_{2.5}$ . WSIIs were largely responsible for  
 277 the variability in  $\text{PM}_{2.5}$ . The ratios of SNA in spring and winter were similar, with ratios of 65.0% for clean days, 75.0% for  
 278 moderate pollution days, and 83.9% for heavy pollution days. With the degradation of air quality, the contribution of  $\text{NO}_3^-$

279 noticeably increased from 27.5% to 47.8% in spring and from 28.9% to 44.7% in autumn. To understand the oxidation rates  
280 of SO<sub>2</sub> and NO<sub>2</sub>, the sulfur oxidation rate and nitrogen oxidation rate (defined as  $SOR = SO_4^{2-}/(SO_4^{2-}+SO_2)$  and  $NOR =$   
281  $NO_3^-/(NO_3^- + NO_2)$ ) were calculated. The critical value of SOR and NOR in the atmosphere are both 0.1 (Win et al., 2020).  
282 The order of the seasonal average NOR was winter (0.21) > spring (0.18) > autumn (0.17) > summer (0.15), while the order  
283 of the seasonal average SOR was winter (0.51) > spring (0.43) > autumn (0.42) > summer (0.36). PM<sub>2.5</sub> pollution in winter is  
284 associated with high RH and rapid production of particulate sulfate from the oxidation of SO<sub>2</sub> emitted by coal combustion  
285 (Wang et al., 2020). From summer to winter, the NOR and SOR values increased by 40.0% and 41.6%, respectively. SOR  
286 and NOR showed a strong positive correlation with relative humidity, with a correlation coefficient of 0.53 and 0.61,  
287 respectively. The contribution of coal combustion varied between 30 and 57% of PM<sub>2.5</sub> in winter (Zhang et al., 2017). Under  
288 the conditions of high coal combustion emissions and high RH, the rapid oxidation of SO<sub>2</sub> occurred to produce sulfate. The  
289 sensitivity of PM<sub>2.5</sub> to surface temperature, wind speed, and boundary layer height is negative, while the sensitivity to  
290 relative humidity is positive (Chen et al., 2018; Sulaymon et al., 2021). In summer, the correlation coefficients of PM<sub>2.5</sub> with  
291 RH, T, WS, and BLH were 0.42, -0.47, -0.15, and -0.23, respectively. In winter, the correlation coefficients of PM<sub>2.5</sub>  
292 concentration with RH, T, WS, and BLH were 0.74, -0.57, -0.31, and -0.32, respectively. High RH (79.6%), low temperature  
293 (4.9°C), low WS (2.1m·s<sup>-1</sup>), and low BLH (419.7m) provided favorable conditions for the accumulation of PM<sub>2.5</sub>.

294 Coal combustion, biomass burning, and motor vehicle emissions all lead to a remarkable increase in carbonaceous  
295 aerosols (Chow et al., 2022). As shown in Figure 2b, carbonaceous species also had a significantly enhanced contribution in  
296 the colder season compared to the warmer season. The seasonal differences might be related to the effects of meteorological  
297 conditions and source emissions. Pearson correlation showed that the relationships between OM and EC and meteorological  
298 parameters (T, RH, WS, and BLH) were not significant (Table 2). To explore the possible pollution sources, it is feasible to  
299 study the mass ratio of OC/EC under different pollution levels. OC comprises thousands of organic compounds. EC is stable  
300 and mainly derived from primary sources of combustion products (Zhang et al., 2017; Wu et al., 2020). The OC/EC mass  
301 ratio of motor vehicle emissions (1.1) is lower than that of coal combustion (2.7) and biomass burning (9.0) (Xu et al., 2021).  
302 In this study, the OC/EC ratios continuously decreased as air pollution got worse, and the values ranged from 6.1 (C), 4.1  
303 (MP) to 3.9 (HP) in spring, from 6.2 (C) to 4.8 (MP) in autumn and from 4.3 (C), 2.7 (MP) to 1.3 (HP) in winter. The annual  
304 average ratio of OC/EC decreased by 56.1% from clean days to heavy pollution days. If the OC/EC values were in the range  
305 of 2.5-5.0, vehicle exhaust emissions were considered as the main source of OC and EC in aerosols, whereas if the OC/EC  
306 values were in the range of 5.0-10.5, coal combustion was considered the main source of OC and EC in aerosols (Gao et al.,  
307 2018; Liu et al., 2018). Distinct differences in the evolution of the OC/EC ratio on polluted days imply that mobile sources  
308 are likely more important. Both the increase in motor vehicle emissions and the formation of meteorological conditions  
309 conducive to pollutant accumulation contribute to the decrease in the OC/EC ratio

310



311  
 312 **Figure 2. Chemical compositions of  $PM_{2.5}$  and mass ratio of OC/EC at different pollution levels of the total samples per season. C,**  
 313 **MP, and HP represent the clean day, moderately polluted day, and heavily polluted day, respectively. “%” represents the**  
 314 **proportion of the filter sample quantity at each pollution level out of the total samples.**

315

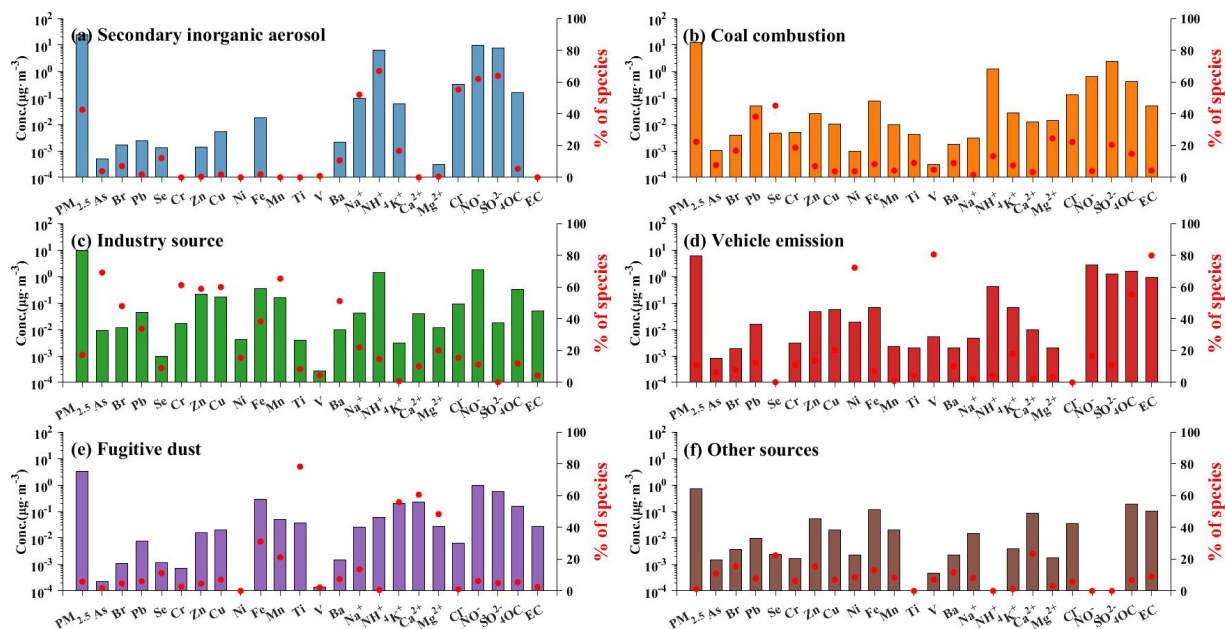
### 316 3.3 Source identification and apportionment

#### 317 3.3.1 Elemental profile and source apportionment from the PMF model

318 To further quantitatively determine the source apportionment of  $PM_{2.5}$ , the EPA PMF5.0 model was adopted. The  
 319 number of factors in the PMF model corresponded to the number of sources of  $PM_{2.5}$  in this study. When the number of  
 320 factors was set to six, the fitting degree of the model calculation results was the highest. Figure 3 presents the factor profiles  
 321 and relative contributions of six factors to each species (% of species total), including secondary inorganic aerosol source  
 322 (SIS), coal combustion (CC), industry source (IS), vehicle emission (VE), fugitive dust (FD), and other sources (OS). The  
 323 meaning of % is the proportion of each chemical component in each source of  $PM_{2.5}$ . As shown in Figure 3a, the  
 324 compositions of SIS were more clear than other sources.  $NO_3^-$  and  $SO_4^{2-}$  are mainly from the oxidation of  $NO_x$  and  $SO_2$ ,  
 325 while  $NH_4^+$  probably comes from the conversion processes between ammonia and sulfuric and nitric acid (Win et al., 2020).  
 326 Factor 1 was identified as the SIS with distinctly high loads of  $NH_4^+$  (66.9%),  $NO_3^-$  (61.9%),  $SO_4^{2-}$  (63.8%) and  $Cl^-$  (55.3%).  
 327 In Figure 3b, the high proportion of Pb (38.2%) and Se (45.1%) was identified in Factor 2, associating with moderate  
 328 weighting on As (14.3%),  $SO_4^{2-}$  (20.5%), and  $Cl^-$  (22.2%). Pb and As are important identifying elements of coal combustion  
 329 and are used as tracers (Xie et al., 2020).  $SO_4^{2-}$  is formed by the photochemical oxidation of sulfur-containing precursors  
 330 ( $SO_2$  and  $H_2S$ ) released by coal combustion (Zong et al., 2016). Given the source profile, Factor 2 was related to coal  
 331 combustion emissions. Factor 3 (Figure 3c) was characterized by the association of heavy metal pollutants such as As  
 332 (42.8%), Pb (33.8%), Cr (61.1%), Zn (58.9%), Cu (59.4%), Fe (38.3%), and Mn (40.1%). As, Pb, Cr, Fe and Mn are related  
 333 to metal smelting and processing (Fang et al., 2021). However, the percentage of OC was only 11.3%, while rates of Zn

334 (58.9%) and Cu (59.4%) were higher in Factor 3 (Fig. 3c). Cu, Zn, and OC are used as tracers of a mixed source of traffic  
 335 and industrial, and OC is the major pollutant in the vehicle exhaust (Wang et al., 2020). Compared to motor vehicle  
 336 emissions, Factor 3 should be significantly influenced by industrial activities. Cu and Zn were mainly from industrial process  
 337 sources. As discussed above, Factor 3 was attributed to the IS. Factor 4 (Figure 3d) was characterized by the association of  
 338 vehicle emissions, with the high proportions of Ni (54.7%), V (80.5%), OC (55.4%), EC (79.8%), and  $\text{NO}_3^-$  (20.3%). VOCs  
 339 and  $\text{NO}_x$  released from vehicles were the precursors of the secondary organic compounds and nitrate in  $\text{PM}_{2.5}$  and were  
 340 important catalysts for increased atmospheric oxidation (Guevara et al., 2021). OC and EC are mainly from the vehicle  
 341 exhaust, and Ni and V are usually tracers of heavy oil combustion (Wu et al., 2020; Veld., 2021). Factor 4 contained a high  
 342 proportion of OC, EC, and  $\text{NO}_3^-$ , which could be considered as vehicle emission, while factor 4 contained Ni and V, which  
 343 were also influenced by shipping emissions (Gao et al., 2018; Veld., 2021). As shown in Figure 3e, Factor 5 had relatively  
 344 high proportions of Fe (31.1%), Ti (78.2%),  $\text{K}^+$  (55.8%),  $\text{Ca}^{2+}$  (60.5%), and  $\text{Mg}^{2+}$  (48.3%). Ti, Fe, and Mg are both common  
 345 crustal elements that can represent the source of mineral dust.  $\text{K}^+$  and  $\text{Ca}^{2+}$  are considered to be significant tracers of biomass  
 346 burning, which have obvious seasonal variations (Tong et al., 2020; Silva et al., 2022). Factor 5 was classified as the fugitive  
 347 dust and biomass burning, including road dust, industrial dust, and soil dust. Factor 6 (Fig. 3f) was unidentified and could be  
 348 affected by coal combustion, industrial processes, and biomass burning. In the absence of a clear designation of the source,  
 349 Factor 6 was attributed to an erroneous contribution from a different source.

350

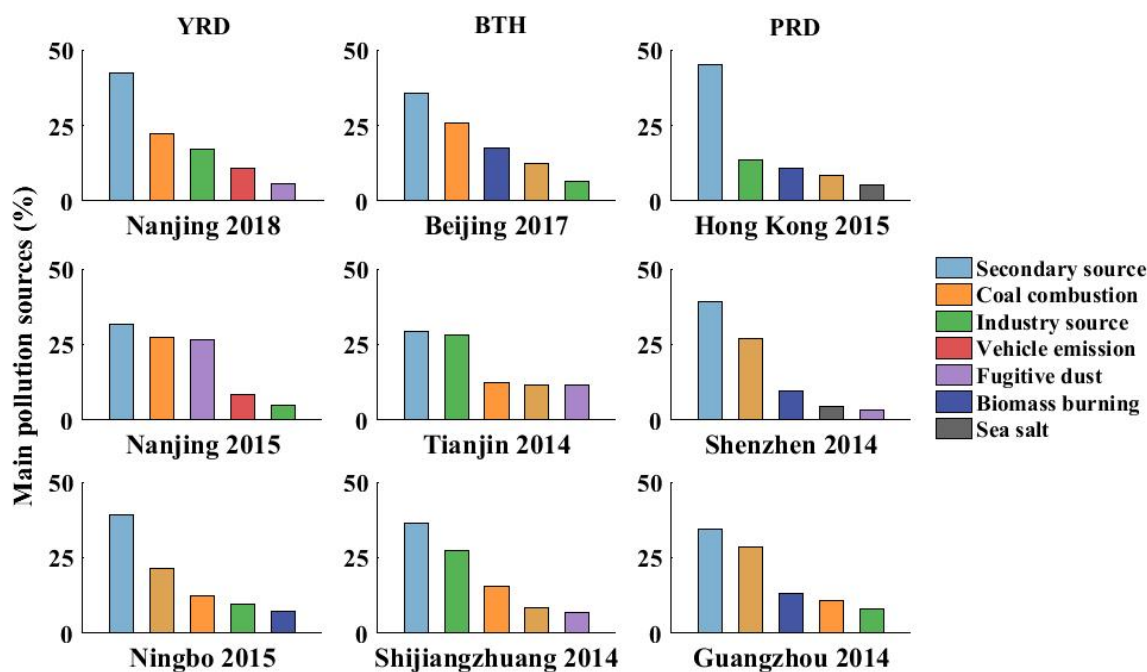


351

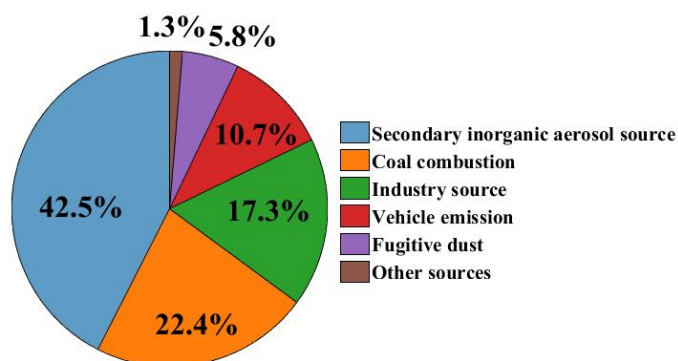
352 **Figure 3. Factor profile in each source for  $\text{PM}_{2.5}$  during the whole year. The histograms are the mass concentration of each species**  
 353 **to every species ( $\mu\text{g}\cdot\text{m}^{-3}$ ), and the red dots are the relative contributions of each source to every species (%).**

354

355 Figure 4 and Figure 5 show the comparisons of our PMF results with the previous findings. In the YED region, SIS  
 356 contributed about 42.5% to  $PM_{2.5}$  in Nanjing in this study, which was higher than that reported by Li et al. (2020), while the  
 357 contributions of CC was lower. However, other sources of  $PM_{2.5}$  in different cities were more complicated. In the BTH, IS  
 358 was crucial source and contributed about 30% of Tianjin and Shijiazhuang (Huang et al., 2017). In contrast, IS in Nanjing  
 359 contributed only 17.3% of  $PM_{2.5}$  pollution. Recent emission control policies in the YRD have had positive effects on  
 360 reducing industrial pollution. In the PRD, vehicle emissions, secondary nitrate, coal burning, and industrial emissions  
 361 showed obvious local emission characteristics. An extra 30%  $PM_{2.5}$  concentration was tightly related to local emissions in  
 362 the downtown and industrial areas (Huang et al., 2014; Li et al., 2020; Chow et al., 2022). In this study, VE contributed only  
 363 10.7% in Nanjing. It is worth noting that the PMF model assumes that source profiles do not change significantly over time  
 364 and that species do not undergo chemical reactions (Paatero and Tapper, 1994). The human activities under seasonal  
 365 variations in this study made the actual pollution incompatible with the ideal assumption. For example, emissions from coal  
 366 combustion increased the contribution of CC in winter significantly (Xu et al., 2021). In addition, the sources of air masses  
 367 in each season also created uncertainties. All of these required detailed discussions of regional transport conditions in each  
 368 season.  
 369



370  
 371 **Figure 4. Comparisons of source apportionment for  $PM_{2.5}$  among different cities.**  
 372



373  
 374 **Figure 5. Average annual contribution of the sources identified for PM<sub>2.5</sub> in Nanjing in 2018.**  
 375

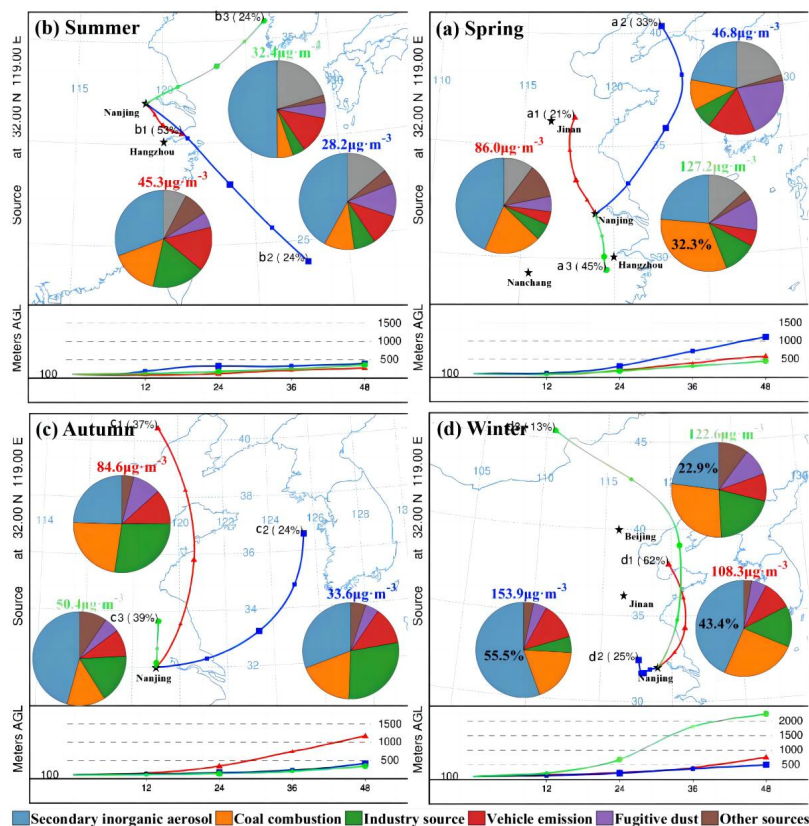
376 **3.3.2 Source identification by backward air mass trajectory analysis**

377 The regional transport of air pollutants exerts a profound impact on local air quality (Shu et al., 2017). Figure 6 shows  
 378 the quantified contributions of PM<sub>2.5</sub> with 48-h backward trajectories. In spring (Fig 6a), nearly half of the air masses (cluster  
 379 a3) stemmed from northern Jiangxi, passed over Anhui Province before arriving at the sampling sites, and had the highest  
 380 PM<sub>2.5</sub> average value (127.2  $\mu\text{g}\cdot\text{m}^{-3}$ ). CC from cluster a3 had the highest contribution with mass and percentage contributions  
 381 being 41.0  $\mu\text{g}\cdot\text{m}^{-3}$  and 32.3%, respectively. In addition, FD contributed relatively highly in clusters a2 and a3, with  
 382 proportions of 18.2% and 10.3%, respectively. Increased contribution from fugitive dust was related to industrial and  
 383 construction activities (Xu et al., 2016). Cluster a2 originated in Liaoning and Cluster a3 was from northern Jiangxi. There  
 384 were many industrial cities located in Liaoning, and the largest coal-fired thermal power plant in Jiangxi was located in the  
 385 northern city of Jiujiang (Xu et al., 2016; Wang et al., 2019). Long-range transport of dust from these areas would have a  
 386 high impact on the formation of severe particle pollution in the YRD. In summer (Fig 6b), the most obvious characteristic of  
 387 regional transport was significantly influenced by the ocean. Clusters b2 and b3 were relatively clean with low  
 388 concentrations of PM<sub>2.5</sub> (28.2  $\mu\text{g}\cdot\text{m}^{-3}$  for b2 and 32.4  $\mu\text{g}\cdot\text{m}^{-3}$  for b3). These clusters passed over the ocean areas and  
 389 accounted for more than half of all trajectories. The magnitude of total CC, IS and VE exhibited a descending order from  
 390 clusters b1 to b3. The dilution effects of clean ocean air masses played a vital role in particulate pollution. In autumn (Fig  
 391 6c), there were the highest concentrations of PM<sub>2.5</sub> in cluster c1, with an average value of 84.6  $\mu\text{g}\cdot\text{m}^{-3}$ . CC (23.1%) and IS  
 392 (27.6%) contributed relatively highly in cluster c1, indicating that regional transport from industrial regions might play an  
 393 important role. For SIS, the proportion of NH<sub>4</sub><sup>+</sup> in these air masses was significantly higher in autumn than those in other  
 394 seasons (Table 2). The increase in the proportion of NH<sub>4</sub><sup>+</sup> indicated that air pollution masses were heavily affected by nearby  
 395 agricultural activities. In winter (Fig 6d), clusters d1 (108.3  $\mu\text{g}\cdot\text{m}^{-3}$ ) and d3 (122.6  $\mu\text{g}\cdot\text{m}^{-3}$ ) originated from Shandong  
 396 Province and the BTH, accounting for more than three-quarters of the air masses. These air masses, which moved at high  
 397 altitudes with a slow speed, could have carried abundant air pollutants. Cluster d2 (153.9  $\mu\text{g}\cdot\text{m}^{-3}$ ) was short-distance  
 398 transport and derived from Jiangsu Province. The contribution of SIS exhibited a increasing order from clusters d1 (22.9%)



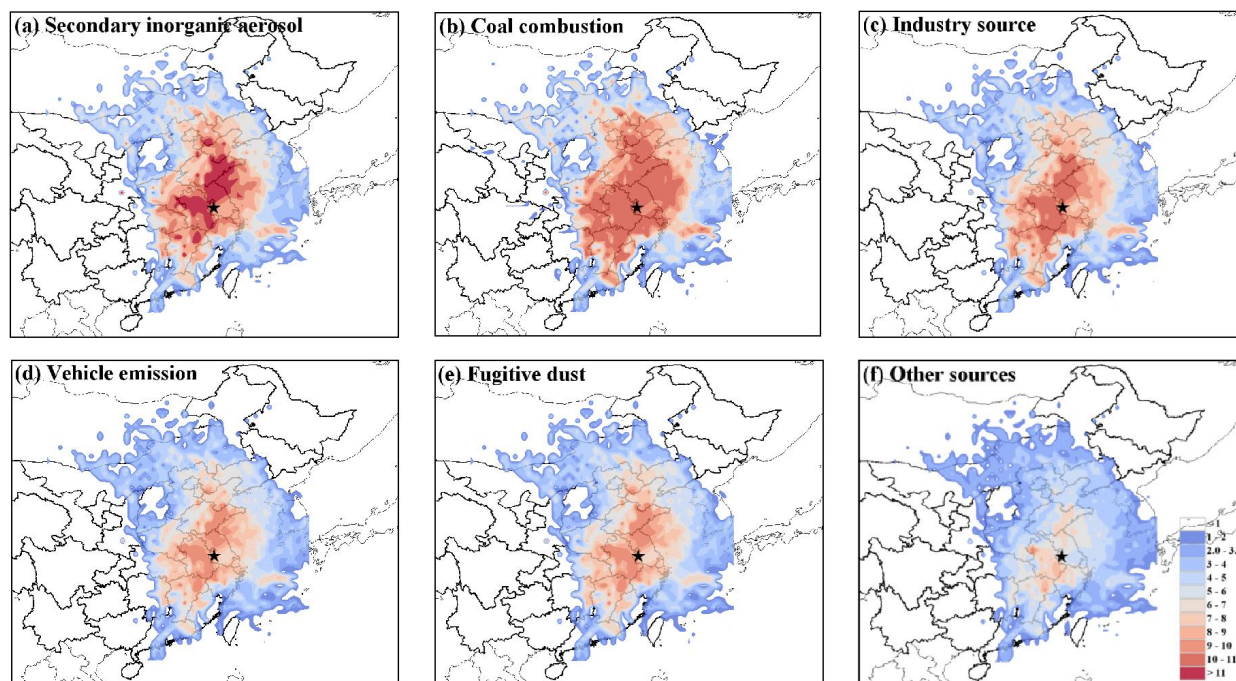
399 to d3 (43.4%) to d2 (55.5%), corresponding to the transition from long-range transport air masses to short-distance transport  
 400 air masses.

401 Figure 7 shows the spatial distribution of the contribution from each source of PM<sub>2.5</sub> by the CWT method and  
 402 highlighted the potential geographic origins. For SIS (Fig. 7a), the high levels (10-15  $\mu\text{g}\cdot\text{m}^{-3}$ ) of this source mainly  
 403 originated from local emissions in Jiangsu and regional transport from Shandong Province. For CC (Fig. 7b), the high  
 404 emissions (10-11  $\mu\text{g}\cdot\text{m}^{-3}$ ) were distributed in the YRD and central China. The weighted concentration values of CC were  
 405 lower than those of the SIS. High concentrations near the center area are associated with local sources, while those far away  
 406 from the center area are indicative of regional transport (Shu et al., 2017). The secondary aerosol source was probably from  
 407 the accumulation of precursors emitted by local emissions. For IS and VE (Fig. 7c and d), there were no high potential areas  
 408 for these sources. The moderate weighted concentration values of IS (8-10  $\mu\text{g}\cdot\text{m}^{-3}$ ) were potentially located in the north of  
 409 Jiangsu, Anhui, and Jiangxi, which were the most important industrial base in China. The oceanic air masses are influenced  
 410 by tropical cyclones with high temperature and strong wind (Li et al., 2018; Chow et al., 2022). Based on the backward  
 411 trajectory calculation, most of the long-range transport of PM<sub>2.5</sub> passed through the Yellow Sea and the East Sea. High wind  
 412 speed had a great effect on mitigating PM<sub>2.5</sub> pollution.



413  
 414 **Figure 6. Source contributions to PM<sub>2.5</sub> grouped by air masses associated with different 48-h backward trajectory clusters. The pie**  
 415 **charts show the average source contribution for corresponding clusters.**





417  
 418 **Figure 7. Potential source regions for individual sources of PM<sub>2.5</sub> identified by the CWT method from March 2018 to February**  
 419 **2019.**

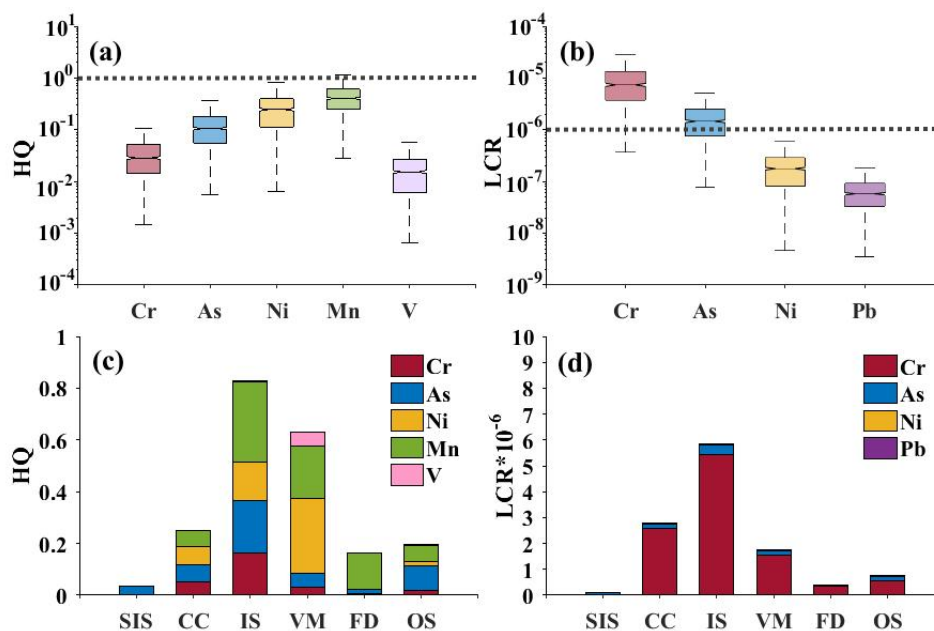
420

### 421 3.4 Non-carcinogenic and carcinogenic health risks of toxic metal elements in each source of PM<sub>2.5</sub>

422 Figure 8 shows the HQ values of non-carcinogenic and the LCR values of carcinogenic risks in PM<sub>2.5</sub> and their total  
 423 health risk in each source. For non-carcinogenic risk (Fig. 8a), the order of the average HQ values was Mn(0.47) > Ni  
 424 (0.32) > As (0.14) > Cr (0.04) > V (0.02). The HQ values of toxic elements were all less than one, which indicated that there  
 425 was no significant non-carcinogenic risk. However, the summation of five HQ values was higher than one, indicating that  
 426 the combined exposure to the pollutant class still had adverse effects. The carcinogenic risk (Fig. 8b) posed by Ni ( $2.3 \times 10^{-7}$ )  
 427 and Pb ( $6.8 \times 10^{-8}$ ) were lower than  $1 \times 10^{-6}$  and could be acceptable. The carcinogenic risk level of Cr ( $1.0 \times 10^{-7}$ ) and As  
 428 ( $1.8 \times 10^{-5}$ ) were within the tolerance or acceptable level ( $1 \times 10^{-6}$ - $1 \times 10^{-4}$ ) (Zheng et al., 2019). Figures 8 c and d show the  
 429 integrated assessment of the source apportionment in toxic elements. IS accounted for the largest proportion of the non-  
 430 carcinogenic and carcinogenic risk, with the HQ of 0.83 and the LCR of  $5.8 \times 10^{-6}$ , respectively. Although the PMF results  
 431 indicated that SIS had the highest contribution to PM<sub>2.5</sub> (Fig. 5), the health risk results showed that the health risks of toxic  
 432 elements from IS and CC were much higher than those from SIS. Previous studies showed that coal combustion sources in  
 433 Beijing, Shanxi, and Jinan had higher respiratory exposure and health risks, while the fugitive dust source in Liaoning  
 434 contained higher levels of Pb, As, and Co (Zeng et al., 2019). As, Cr, and Ni in PM<sub>2.5</sub> were within the acceptable level for  
 435 both children and adults in Nanjing, but there was a potential carcinogenic risk posed by Pb via ingestion to children and

436 adults (Hu et al., 2012). It was related to the differences in PM<sub>2.5</sub> pollution characteristics and source contributions in  
 437 different cities. The ingestion exposure may result in the potential health risk from IS, CC, and VE. Based on the  
 438 implementation of energy conservation and emission reduction policies, the main source of pollution in Nanjing is SIS at  
 439 present, and the health risk has been alleviated. However, we should pay more attention to the health burden of vehicle  
 440 emissions, coal combustion, and industrial processes.

441



442

443 **Figure 8. Non-carcinogenic (a) and carcinogenic (b) risks of toxic elements. Non-carcinogenic (c) and carcinogenic (d) risk of the**  
 444 **sources identified for PM<sub>2.5</sub> in Nanjing. HQ, LCR, SIS, CC, IS, VM, FD, and OS represent hazard quotient, lifetime carcinogenic**  
 445 **risk, secondary inorganic aerosol source, coal combustion, industry source, vehicle emission, fugitive dust, and other sources,**  
 446 **respectively.**

447

### 448 3. Conclusions

449 Identifying and quantitatively assessing the contributions and health risks of pollution sources has played an important  
 450 role in formulating policies to control particle pollution. We have derived a high-quality PM<sub>2.5</sub> composition data set, based  
 451 on a chemical component monitoring from March 2018 to February 2019 in Nanjing. The PMF and back-trajectory results  
 452 were adopted to investigate the chemical characteristics and regional transports of each source. The health risk assessment  
 453 was used to explore non-carcinogenic and carcinogenic risks of toxic elements.

454 The results showed that PM<sub>2.5</sub> concentrations ranged from 6.7 to 234.0  $\mu\text{g}\cdot\text{m}^{-3}$ , with an annual average of 68.7  $\mu\text{g}\cdot\text{m}^{-3}$ .  
 455 Water-soluble ions contributed the most to PM<sub>2.5</sub>. From summer to winter, the  $\text{NO}_3^-/\text{SO}_4^{2-}$  ratio increased from 1.2 to 1.59.  
 456 OC/EC ratio decreased by 56.1% from clean days to heavy pollution days. The average OC/EC ratio on heavy pollution days

457 was 1.3. Both the increase in motor vehicle emissions and the formation of meteorological conditions conducive to pollutant  
458 accumulation contribute to the decrease in the OC/EC ratio. Based on the PMF model, the source variations and health risks  
459 were assessed. The contribution of identified sources (including SIS (42.5%), CC (22.4%), IS (17.3%), VE (10.7%), FD  
460 (5.8%), and other sources (1.3%)) had different spatial distributions and seasonal variations. The CWT analysis indicated  
461 that high emissions (10-11  $\mu\text{g}\cdot\text{m}^{-3}$ ) of SIS and CC were distributed in the YRD and central China in winter. Moderate  
462 emissions (8-9  $\mu\text{g}\cdot\text{m}^{-3}$ ) of IS and VE were potentially located in the north of Jiangsu, Anhui, and Jiangxi. The carcinogenic  
463 and non-carcinogenic risks of toxic elements (Cr, As, Ni, Mn, V, and Pb) mainly came from IS, VE, and CC, which were  
464 within the tolerance or acceptable level. Based on the implementation of energy conservation and emission reduction  
465 policies, the main source of pollution in Nanjing is SIS at present, and the health risk has been alleviated. However, we  
466 should pay more attention to the health burden of vehicle emissions, coal combustion, and industrial processes.

467 This study provided new insight for PM<sub>2.5</sub> research between the source apportionment and health risk. The results  
468 presented characteristics of chemical components, pinpointed secondary transformation processes leading to the high PM<sub>2.5</sub>  
469 concentrations, revealed spatial variations of source contribution, and provided new references for mega-cities to conduct  
470 health risk analysis on air pollution control measures.

471

#### 472 ***Data Availability.***

473 PM<sub>2.5</sub> composition data were collected by the atmospheric heavy metal Monitor and the In-situ Gas and Aerosol  
474 Compositions Monitor in the School of Atmospheric Sciences, Nanjing University (The data presented in this article are  
475 available upon request from Yangzhihao Zhan (zyzh1049744276@gmail.com)). Air quality monitoring data were acquired  
476 from the official NEMC real-time publishing platform (<https://air.cnemc.cn:18007/>, last access: 7 April 2023).  
477 Meteorological data were obtained from the University of Wyoming website (<http://weather.uwyo.edu/>, last access: 7 April  
478 2023). The NCEP FNL data were taken from the NCEP (<https://rda.ucar.edu/datasets/>, last access: 7 April 2023). These data  
479 can be downloaded for free as long as one agrees to the official instructions.

480

#### 481 ***Author contributions.***

482 YZ and MX had original ideas, designed the research, collected the data, and prepared the original draft. YZ, WZ, PC, YL,  
483 and RZ performed PMF experiments and carried out the data analysis. MX and WZ acquired financial support for the project  
484 leading to this publication. TW, DG, JT, KZ, SL, BZ, and ML reviewed the initial draft and checked the English of the  
485 original paper.

486

#### 487 ***Acknowledgments.***

488 The authors are grateful to NEMC for the air quality monitoring data, to NCDC for the meteorological data, and to NCEP for  
489 global final analysis fields. We gratefully acknowledge the NOAA Air Resources Laboratory (ARL) for providing the

490 HYSPLIT transport and dispersion model used in this work. We acknowledge the Chinese Academy of Meteorological  
491 Sciences for supporting this work (<http://www.meteothink.org/>, last access: 7 April 2023).

492

493 ***Competing interests.***

494 The contact author has declared that neither they nor their co-author has any competing interests.

495

496 ***Financial support.***

497 This research has been supported by the Natural Science Foundation of Jiangsu Province (grant no. BK20211158), the  
498 National Nature Science Foundation of China (grant no. 42275102), and the Basic Special Business Fund for R&D for the  
499 Central Level Scientific Research Institutes of Nanjing Institute of Environmental Sciences (grant no. GYZX210501)

500 **References**

501 Andreae, M. O.: Emission of trace gases and aerosols from biomass burning an updated assessment, *Atmos. Chem. Phys.*,  
502 19, 8523 – 8546, <https://doi.org/10.5194/acp-19-8523-2019>, 2019.

503 Behrooz, R. D., Kaskaoutis, D. G., Grivas, G., and Mihalopoulos, N.: Human health risk assessment for toxic elements in the  
504 extreme ambient dust conditions observed in Sistan, Iran, *Chemosphere*, 262,  
505 <https://doi.org/10.1016/j.chemosphere.2020.127835>, 2021.

506 Brokamp, C., Jandarov, R., Rao, M. B., LeMasters, G., and Ryan, P.: Exposure assessment models for elemental components  
507 of particulate matter in an urban environment: A comparison of regression and random forest approaches, *Atmos.*  
508 *Environ.*, 151, 1-11, <https://doi.org/10.1016/j.atmosenv.2016.11.066>, 2017.

509 Chen, D., Cui, H. F., Zhao, Y., Yin, L. N., Lu, Y., and Wang, Q. G.: A two-year study of carbonaceous aerosols in ambient  
510 PM<sub>2.5</sub> at a regional background site for western Yangtze River Delta, China, *Atmos. Res.*, 183, 351-361,  
511 <https://doi.org/10.1016/j.atmosres.2016.09.004>, 2017.

512 Chen, Z. Y., Xie, X. M., Cai, J., Chen, D. L., Gao, B. B., He, B., Cheng, N. L., and Xu, B.: Understanding meteorological  
513 influences on PM<sub>2.5</sub> concentrations across China: a temporal and spatial perspective, *Atmos. Chem. Phys.*, 18, 5343-5358,  
514 <https://doi.org/10.5194/acp-18-5343-2018>, 2018.

515 Cheng, J., Tong, D., Zhang, Q., Liu, Y., Lei, Y., Yan, G., Yan, L., Yu, S., Cui, Y. R., Clarke, L., Geng, G. G., Zheng, B.,  
516 Zhang, X. T., Davis, S. J., He, K. B.: Pathways of China's PM<sub>2.5</sub> air quality 2015–2060 in the context of carbon neutrality.  
517 *National Science Review*, 8(12), nwab078, <https://doi.org/10.1093/nsr/nwab078>, 2021.

518 Chow, W. S., Huang, X. H. H., Leung, K. F., Huang, L., Wu, X. R., and Yu, J. Z.: Molecular and elemental marker-based  
519 source apportionment of fine particulate matter at six sites in Hong Kong, China, *Sci. Total Environ.*, 813,  
520 <https://doi.org/10.1016/j.scitotenv.2021.152652>, 2022.

521 Conibear, L., Butt, E. W., Knote, C., Arnold, S. R., and Spracklen, D. V.: Residential energy use emissions dominate health  
522 impacts from exposure to ambient particulate matter in India. *Nature communications*, 9(1), 617,  
523 <https://doi.org/10.1038/s41467-018-02986-7>, 2018.

524 Fan, H., Zhao, C. F., and Yang, Y. K.: A comprehensive analysis of the spatio-temporal variation of urban air pollution in  
525 China during 2014-2018, *Atmos. Environ.*, 220, <https://doi.org/10.1016/j.atmosenv.2019.117066>, 2020.

526 Fang, B., Zeng, H., Zhang, L., Wang, H. W., Liu, J. J., Hao, K. L., Zheng, G. Y., Wang, M. M., Wang, Q., and Yang, W. Q.:  
527 Toxic metals in outdoor/indoor airborne PM<sub>2.5</sub> in port city of Northern, China: Characteristics, sources, and personal  
528 exposure risk assessment, *Environ. Pollut.*, 279, <https://doi.org/10.1016/j.envpol.2021.116937>, 2021.

529 Feng, X. Y., Tian, Y. Z., Xue, Q. Q., Song, D. L., Huang, F. X., and Feng, Y. C.: Measurement report: Spatiotemporal and  
530 policy-related variations of PM<sub>2.5</sub> composition and sources during 2015-2019 at multiple sites in a Chinese megacity,  
531 *Atmos. Chem. Phys.*, 21, 16219-16235, <https://doi.org/10.5194/acp-21-16219-2021>, 2021.

532 Gao, D., Xie, M., Liu, J., Wang, T. J., Ma, C. Q., Bai, H. K., Chen, X., Li, M. M., Zhuang, B. L., and Li, S.: Ozone  
533 variability induced by synoptic weather patterns in warm seasons of 2014-2018 over the Yangtze River Delta region,  
534 *China, Atmos. Chem. Phys.*, 21, 5847-5864, <https://doi.org/10.5194/acp-21-5847-2021>, 2021.

535 Gao, J. J., Wang, K., Wang, Y., Liu, S. H., Zhu, C. Y., Hao, J. M., Liu, H. J., Hua, S. B., Tian, H. Z.: Temporal-spatial  
536 characteristics and source apportionment of PM<sub>2.5</sub> as well as its associated chemical species in the Beijing-Tianjin-Hebei  
537 region of China, *Environ. Pollut.*, 233, 714-724, <https://doi.org/10.1016/j.envpol.2017.10.123>, 2018.

538 Guevara, M., Jorba, O., Soret, A., Petetin, H., Bowdalo, D., Serradell, K., Tena, C., van der Gon, H. D., Kuenen, J., Peuch, V.  
539 H., and Garcia-Pando, C. P.: Time-resolved emission reductions for atmospheric chemistry modelling in Europe during  
540 the COVID-19 lockdowns, *Atmos. Chem. Phys.*, 21, 773-797, <https://doi.org/10.5194/acp-21-773-2021>, 2021.

541 Hayes, R. B., Lim, C., Zhang, Y., Cromar, K., Shao, Y., Reynolds, H. R., Silverman, D. T., Jones, R. R., Park, Y., Jerrett, M.,  
542 Ahn, J., and Thurston, G. D.: PM<sub>2.5</sub> air pollution and cause-specific cardiovascular disease mortality. *International journal*  
543 *of epidemiology*, 49(1), 25-35, <https://doi.org/10.1093/ije/dyz114>, 2019.

544 Hu, X., Zhang, Y., Ding, Z. H., Wang, T. J., Lian, H. Z., Sun, Y. Y., and Wu, J. C.: Bioaccessibility and health risk of  
545 arsenic and heavy metals (Cd, Co, Cr, Cu, Ni, Pb, Zn and Mn) in TSP and PM<sub>2.5</sub> in Nanjing, China, *Atmos. Environ.*, 57,  
546 146-152, <https://doi.org/10.1016/j.atmosenv.2012.04.056>, 2012.

547 Huang, X. F., Yun, H., Gong, Z. H., Li, X., He, L. Y., Zhang, Y. H., and Hu, M.: Source apportionment and secondary  
548 organic aerosol estimation of PM<sub>2.5</sub> in an urban atmosphere in China. *Sci. China Earth Sci.* 57, 1352–1362 (2014).  
549 <https://doi.org/10.1007/s11430-013-4686-2>, 2014.

550 Huang, X. J., Liu, Z. R., Liu, J. Y., Hu, B., Wen, T. X., Tang, G. Q., Zhang, J. K., Wu, F. K., Ji, D. S., Wang, L. L., and  
551 Wang, Y. S.: Chemical characterization and source identification of PM<sub>2.5</sub> at multiple sites in the Beijing-Tianjin-Hebei  
552 region, China, *Atmos. Chem. Phys.*, 17, 12941-12962, <https://doi.org/10.5194/acp-17-12941-2017>, 2017.

553 Islam, M. R., Jayarathne, T., Simpson, I. J., Werden, B., Maben, J., Gilbert, A., Praveen, P. S., Adhikari, S., Panday, A. K.,  
554 Rupakheti, M., Blake, D. R., Yokelson, R. J., DeCarlo, P. F., Keene, W. C., and Stone, E. A.: Ambient air quality in the

555 Kathmandu Valley, Nepal, during the pre-monsoon: concentrations and sources of particulate matter and trace gases,  
556 *Atmos. Chem. Phys.*, 20, 2927-2951, <https://doi.org/10.5194/acp-20-2927-2020>, 2020.

557 Jeong, C. H., Wang, J. M., Hilker, N., Deboisz, J., Sofowote, U., Su, Y., Noble, M., Healy, R., Munoz, T., Celo, V., White, L.,  
558 Audette, C., Herod, D., and Evans, G. J.: Temporal and spatial variability of traffic-related PM<sub>2.5</sub> sources: Comparison of  
559 exhaust and non-exhaust emissions, *Atmos. Environ.*, 198, 55-69. <https://doi.org/10.1016/j.atmosenv.2018.10.038>, 2019.

560 Jiang, N., Duan, S. G., Yu, X., Zhang, R. Q., and Wang, K.: Comparative major components and health risks of toxic  
561 elements and polycyclic aromatic hydrocarbons of PM<sub>2.5</sub> in winter and summer in Zhengzhou: Based on three-year data,  
562 *Atmos. Res.*, 213, 173-184, <https://doi.org/10.1016/j.atmosres.2018.06.008>, 2018.

563 Khan, M. F., Latif, M. T., Saw, W. H., Amil, N., Nadzir, M. S. M., Sahani, M., Tahir, N. M., and Chung, J. X.: Fine  
564 particulate matter in the tropical environment: monsoonal effects, source apportionment, and health risk assessment,  
565 *Atmos. Chem. Phys.*, 16, 597-617, <https://doi.org/10.5194/acp-16-597-2016>, 2016.

566 Kumari, P., and Toshniwal, D.: Impact of lockdown measures during COVID-19 on air quality- A case study of India, *Int. J.*  
567 *Environ. Health Res.*, 32, 503-510, <https://doi.org/10.1080/09603123.2020.1778646>, 2022.

568 Li, M., Hu, M., Guo, Q., Tan, T., Du, B., Huang, X., He, L., Guo, S., Wang, W., Fan, Y. and Xu, D.: Seasonal Source  
569 Apportionment of PM<sub>2.5</sub> in Ningbo, a Coastal City in Southeast China, *Aerosol Air Qual. Res.*, 18: 2741-2752.  
570 <https://doi.org/10.4209/aaqr.2018.01.0011>, 2018.

571 Li, S. W., Chang, M. H., Li, H. M., Cui, X. Y., and Ma, L. Q.: Chemical compositions and source apportionment of PM<sub>2.5</sub>  
572 during clear and hazy days: Seasonal changes and impacts of Youth Olympic Games. *Chem.*, 256, 127163,  
573 <https://doi.org/10.1016/j.chemosphere.2020.127163>, 2020.

574 Li, T. T., Li, J., Jiang, H. X., Chen, D. H., Zong, Z., Tian, C. G., and Zhang, G.: Source Apportionment of PM(2.5)in  
575 Guangzhou Based on an Approach of Combining Positive Matrix Factorization with the Bayesian Mixing Model and  
576 Radiocarbon, *Atmos*, 11, <https://doi.org/10.3390/atmos11050512>, 2020.

577 Li, X. Y., Cheng, T. H., Shi, S. Y., Guo, H., Wu, Y., Lei, M., Zuo, X., Wang, W. N., and Han, Z. Y.: Evaluating the impacts  
578 of burning biomass on regional transport under various emission conditions, *Sci. Total Environ.*, 793,  
579 <https://doi.org/10.1016/j.scitotenv.2021.148481>, 2021.

580 Li, X., Yan, C. Q., Wang, C. Y., Ma, J. J., Li, W. X., Liu, J. Y., and Liu, Y.: PM<sub>2.5</sub>-bound elements in Hebei Province,  
581 China: Pollution levels, source apportionment and health risks, *Sci. Total Environ.*, 806,  
582 <https://doi.org/10.1016/j.scitotenv.2021.150440>, 2022.

583 Liu, J., Wu, D., Fan, S. J., Mao, X., and Chen, H. Z.: A one-year, on-line, multi-site observational study on water-soluble  
584 inorganic ions in PM<sub>2.5</sub> over the Pearl River Delta region, China, *Sci. Total Environ.*, 601, 1720-1732,  
585 <https://doi.org/10.1016/j.scitotenv.2017.06.039>, 2017.

586 Liu, Y. K., Yu, Y. P., Liu, M., Lu, M., Ge, R. R., Li, S. W., Liu, X. R., Dong, W. B., and Qadeer, A.: Characterization and  
587 source identification of PM<sub>2.5</sub>-bound polycyclic aromatic hydrocarbons (PAHs) in different seasons from Shanghai,  
588 China, *Sci. Total Environ.*, 644, 725-735, <https://doi.org/10.1016/j.scitotenv.2018.07.049>, 2018.

589 Liu, Z. R., Gao, W. K., Yu, Y. C., Hu, B., Xin, J. Y., Sun, Y., Wang, L. L., Wang, G. H., Bi, X. H., Zhang, G. H., Xu, H. H.,  
590 Cong, Z. Y., He, J., Xu, J. S., and Wang, Y. S.: Characteristics of PM<sub>2.5</sub> mass concentrations and chemical species in  
591 urban and background areas of China: Emerging results from the CARE-China network. *Atmos. Chem. Phys.*, 18(12),  
592 8849-8871, <https://doi.org/10.5194/acp-18-8849-2018>, 2018.

593 Liu, M. X., Huang, X., Song, Y., Tang, J., Cao, J. J., Zhang, X. Y., Zhang, Q., Wang, S. X., Xu, T. T., Kang, L., Cai, X. H.,  
594 Zhang, H. S., Yang, F. M., Wang, H. B., Yu, J. Z., Lau, A. K. H., He, L. Y., Huang, X. F., Duan, L., Ding, A. J., Xue, L.  
595 K., Gao, J., Liu, B., and Zhu, T.: Ammonia emission control in China would mitigate haze pollution and nitrogen  
596 deposition, but worsen acid rain, *Proc. Natl. Acad. Sci. U. S. A.*, 116, 7760-7765,  
597 <https://doi.org/10.1073/pnas.1814880116>, 2019.

598 Liu, L., Zhang, J., Du, R. G., Teng, X. M., Hu, R., Yuan, Q., Tang, S. S., Ren, C. H., Huang, X., Xu, L., Zhang, Y. X.,  
599 Zhang, X. Y., Song, C. B., Liu, B., Lu, G. D., Shi, Z. B., and Li, W. J.: Chemistry of atmospheric fine particles during the  
600 COVID - 19 pandemic in a megacity of Eastern China. *Geophys. Res.-Atmos.*, 48(2), 2020GL091611,  
601 <https://doi.org/10.1029/2020GL091611>, 2020

602 Lv, Z. F., Wang, X. T., Deng, F. Y., Ying, Q., Archibald, A. T., Jones, R. L., Ding, Y., Cheng, Y., Fu, M. L., Liu, Y., Man,  
603 H. Y., Xue, Z. G., He, K. B., Hao, J. M., and Liu, H. A.: Source-Receptor Relationship Revealed by the Halted Traffic and  
604 Aggravated Haze in Beijing during the COVID-19 Lockdown, *Environ. Sci. Technol.*, 54, 15660-15670,  
605 <https://doi.org/10.1021/acs.est.0c04941>, 2020.

606 Lv, L. L., Wei, P., Hu, J. N., Chen, Y. J., and Shi, Y. P.: Source apportionment and regional transport of PM<sub>2.5</sub> during haze  
607 episodes in Beijing combined with multiple models, *Atmos. Res.*, 266, <https://doi.org/10.1016/j.atmosres.2021.105957>,  
608 2022.

609 Nie, D. Y., Chen, M. D., Wu, Y., Ge, X. L., Hu, J. L., Zhang, K., and Ge, P. X.: Characterization of Fine Particulate Matter  
610 and Associated Health Burden in Nanjing, *Int. J. Env. Res. Public Health*, 15, <https://doi.org/10.3390/ijerph15040602>,  
611 2018.

612 Paatero, P., and Tapper, U.: POSITIVE MATRIX FACTORIZATION - A NONNEGATIVE FACTOR MODEL WITH  
613 OPTIMAL UTILIZATION OF ERROR-ESTIMATES OF DATA VALUES, *Environmetrics*, 5, 111-126,  
614 <https://doi.org/10.1002/env.3170050203>, 1994.

615 Sharma, S., Zhang, M. Y., Anshika, Gao, J. S., Zhang, H. L., and Kota, S. H.: Effect of restricted emissions during COVID-  
616 19 on air quality in India, *Sci. Total Environ.*, 728, <https://doi.org/10.1016/j.scitotenv.2020.138878>, 2020.

617 Shu, L., Xie, M., Gao, D., Wang, T. J., Fang, D. X., Liu, Q., Huang, A. N., and Peng, L. W.: Regional severe particle  
618 pollution and its association with synoptic weather patterns in the Yangtze River Delta region, China, *Atmos. Chem. Phys.*,  
619 17, 12871-12891, <https://doi.org/10.5194/acp-17-12871-2017>, 2017.

620 Silva, L. F., Schneider, I. L., Artaxo, P., Núñez-Blanco, Y., Pinto, D., Flores, É. M., Gómez-Plata, L., Ramírez, O., and  
621 Dotto, G. L.: Particulate matter geochemistry of a highly industrialized region in the Caribbean: Basis for future  
622 toxicological studies, *Geos. Front*, 13(1), 101-115, <https://doi.org/10.1016/j.gsf.2020.11.012>, 2022.

623 Song, C. B., He, J. J., Wu, L., Jin, T. S., Chen, X., Li, R. P., Ren, P. P., Zhang, L., and Mao, H. J.: Health burden attributable  
624 to ambient PM<sub>2.5</sub> in China. *Environ., Pollut.*, 223, 575-586, <https://doi.org/10.1016/j.envpol.2017.01.060>, 2017.

625 Sulaymon, I. D., Zhang, Y. X., Hopke, P. K., Zhang, Y., Hua, J. X., and Mei, X. D.: COVID-19 pandemic in Wuhan:  
626 Ambient air quality and the relationships between criteria air pollutants and meteorological variables before, during, and  
627 after lockdown, *Atmos. Res.*, 250, <https://doi.org/10.1016/j.atmosres.2020.105362>, 2021.

628 Tao, J., Zhang, L., Cao, J., and Zhang, R.: A review of current knowledge concerning PM<sub>2.5</sub> chemical composition, aerosol  
629 optical properties and their relationships across China, *Atmos. Chem. Phys.*, 17, 9485–9518, [https://doi.org/10.5194/acp-](https://doi.org/10.5194/acp-17-9485-2017)  
630 [17-9485-2017](https://doi.org/10.5194/acp-17-9485-2017), 2017.

631 Taylor, A. A., Tsuji, J. S., Garry, M. R., McArdle, M. E., Goodfellow, W. L., Adams, W. J., and Menzie, C. A.: Critical  
632 Review of Exposure and Effects: Implications for Setting Regulatory Health Criteria for Ingested Copper, *Environ.*  
633 *Manage.*, 65, 131-159, <https://doi.org/10.1007/s00267-019-01234-y>, 2020.

634 Thurston, G. D., Burnett, R. T., Turner, M. C., Shi, Y., Krewski, D., Lall, R., Ito, K., Jerrett, M., Gapstur, S. M., Diver, W.  
635 R., and Pope III, C. A.: Ischemic heart disease mortality and long-term exposure to source-related components of US fine  
636 particle air pollution. *Environ. Health Pers.*, 124(6), 785-794, <https://doi.org/10.1289/ehp.1509777>, 2016.

637 Tong, S. Y., Kong, L. D., Yang, K. J., Shen, J. D., Chen, L., Jin, S. Y., Wang, C., Sha, F., and Wang, L.: Characteristics of  
638 air pollution episodes influenced by biomass burning pollution in Shanghai, China, *Atmos. Environ.*, 238,  
639 <https://doi.org/10.1016/j.atmosenv.2020.117756>, 2020.

640 Tseng, C. H., Tsuang, B. J., Chiang, C. J., Ku, K. C., Tseng, J. S., Yang, T. Y., Hsu, K. H., Chen, K. C., Yu, S. L., Lee, W.  
641 C., Liu, T. W., Chan, C. C., and Chang, G. C.: The Relationship Between Air Pollution and Lung Cancer in Nonsmokers  
642 in Taiwan, *J. Thorac. Oncol.*, 14, 784-792, <https://doi.org/10.1016/j.jtho.2018.12.033>, 2019.

643 Veld, M., Alastuey, A., Pandolfi, M., Amato, F., Perez, N., Reche, C., and Querol, X.: Compositional changes of PM<sub>2.5</sub> in  
644 NE Spain during 2009–2018: A trend analysis of the chemical composition and source apportionment, *Sci. Total Environ.*,  
645 795, 148728, <https://doi.org/10.1016/j.scitotenv.2021.148728>, 2021.

646 Wang, S. S., Hu, G. R., Yan, Y., Wang, S., Yu, R. L., and Cui, J. Y.: Source apportionment of metal elements in PM<sub>2.5</sub> in a  
647 coastal city in Southeast China: Combined Pb-Sr-Nd isotopes with PMF method, *Atmos. Environ.*, 198, 302-312,  
648 <https://doi.org/10.1016/j.atmosenv.2018.10.056>, 2019.

649 Wang, S. B., Ji, Y. Q., Zhao, J. B., Lin, Y., and Lin, Z.: Source apportionment and toxicity assessment of PM<sub>2.5</sub>-bound PAHs  
650 in a typical iron-steel industry city in northeast China by PMF-ILCR, *Sci. Total Environ.*, 713,  
651 <https://doi.org/10.1016/j.scitotenv.2019.136428>, 2020.

652 Wang, J. F., Li, J. Y., Ye, J. H., et al.: Fast sulfate formation from oxidation of SO<sub>2</sub> by NO<sub>2</sub> and HONO observed in Beijing  
653 haze. *Nat. Commun.*, 11(1), 2844, <https://doi.org/10.1038/s41467-020-16683-x>, 2020.

654 Wang, H. L., Ke, Y., Tan, T., Zhu, B., Zhao, L. T., Yin, Y.: Observational evidence for the dual roles of BC in the megacity  
655 of eastern China: Enhanced O<sub>3</sub> and decreased PM<sub>2.5</sub> pollution, *Chemosphere*, 327,  
656 <https://doi.org/10.1016/j.chemosphere.2023.138548>, 2023.



657 Win, M. S., Zeng, J. Y., Yao, C. H., Zhao, M. F., Xiu, G. L., Xie, T. T., Rao, L. F., Zhang, L. Y., Lu, H., Liu, X. C., Wang,  
658 Q. Y., and Lu, S. N.: Sources of HULIS-C and its relationships with trace metals, ionic species in PM<sub>2.5</sub> in suburban  
659 Shanghai during haze and non-haze days, *JAtC*, 77, 63-81, <https://doi.org/10.1007/s10874-020-09404-7>, 2020.

660 Wong, Y. K., Liu, K. M., Yeung, C., Leung, K. K. M., and Yu, J. Z.: Measurement report: Characterization and source  
661 apportionment of coarse particulate matter in Hong Kong: insights into the constituents of unidentified mass and source  
662 origins in a coastal city in southern China, *Atmos. Chem. Phys.*, 22, 5017-5031, <https://doi.org/10.5194/acp-22-5017-2022>,  
663 2022.

664 Wu, X., Cao, F., Haque, M., Fan, M. Y., Zhang, S. C., and Zhang, Y. L.: Molecular composition and source apportionment  
665 of fine organic aerosols in Northeast China, *Atmos. Environ.*, 239, <https://doi.org/10.1016/j.atmosenv.2020.117722>, 2020.

666 Xie, M., Liao, J. B., Wang, T. J., Zhu, K. G., Zhuang, B. L., Han, Y., Li, M. M., and Li, S.: Modeling of the anthropogenic  
667 heat flux and its effect on regional meteorology and air quality over the Yangtze River Delta region, China, *Atmos. Chem.*  
668 *Phys.*, 16, 6071-6089, <https://doi.org/10.5194/acp-16-6071-2016>, 2016.

669 Xie, J. J., Yuan, C. G., Xie, J., Niu, X. D., and He, A. E.: PM<sub>2.5</sub>-bound potentially toxic elements (PTEs) fractions,  
670 bioavailability and health risks before and after coal limiting, *Ecotoxicol. Environ. Saf.*, 192,  
671 <https://doi.org/10.1016/j.ecoenv.2020.110249>, 2020.

672 Xu, H. M., Cao, J. J., Chow, J. C., Huang, R. J., Shen, Z., Chen, L. A., Ho, K. F. and Watson, J. G.: Inter-annual variability  
673 of wintertime PM<sub>2.5</sub> chemical composition in Xi'an, China: evidences of changing source emissions, *Sci. Total Environ.*,  
674 545, 546-555, <https://doi.org/10.1016/j.scitotenv.2015.12.070>, 2016.

675 Xu, J. S., Liu, D., Wu, X. F., Vu, T., Zhang, Y. L., Fu, P. Q., Sun, Y. L., Xu, W. Q., Zheng, B., Harrison, R. M., and Shi, Z.  
676 B.: Source apportionment of fine organic carbon at an urban site of Beijing using a chemical mass balance model, *Atmos.*  
677 *Chem. Phys.*, 21, 7321-7341, <https://doi.org/10.5194/acp-21-7321-2021>, 2021.

678 Yan, Y., Zheng, Q., Yu, R. L., Hu, G. R., Huang, H. B., Lin, C. Q., Cui, J. Y., and Yan, Y.: Characteristics and provenance  
679 implications of rare earth elements and Sr-Nd isotopes in PM<sub>2.5</sub> aerosols and PM<sub>2.5</sub> fugitive dusts from an inland city of  
680 southeastern China, *Atmos. Environ.*, 220, <https://doi.org/10.1016/j.atmosenv.2019.117069>, 2020.

681 Yan, Y. C., Liu, Z. R., Gao, W., Li, J. Y., Zhang, X. H., Chai, W. H., Bai, J. H., Hu, B., and Wang, Y. S.: Physiochemistry  
682 characteristics and sources of submicron aerosols at the background area of North China Plain: Implication of air pollution  
683 control in heating season, *Atmos. Res.*, 249, <https://doi.org/10.1016/j.atmosres.2020.105291>, 2021.

684 Zeng, Y. Y., Cao, Y. F., Qiao, X., Seyler, B. C., and Tang, Y.: Air pollution reduction in China: Recent success but great  
685 challenge for the future, *Sci. Total Environ.*, 663, 329-337, <https://doi.org/10.1016/j.scitotenv.2019.01.262>, 2019.

686 Zhan, Y. Z. H., Xie, M., Gao, D., Wang, T. J., Zhang, M., and An, F. X.: Characterization and source analysis of water-  
687 soluble inorganic ionic species in PM<sub>2.5</sub> during a wintertime particle pollution episode in Nanjing, China, *Atmos. Res.*,  
688 262, <https://doi.org/10.1016/j.atmosres.2021.105769>, 2021.

689 Zhang, L. L., Wilson, J. P., MacDonald, B., Zhang, W. H., and Yu, T.: The changing PM<sub>2.5</sub> dynamics of global megacities  
690 based on long-term remotely sensed observations, *Environ. Int.*, 142, <https://doi.org/10.1016/j.envint.2020.105862>, 2020.

691 Zhang, Z. Z., Wang, W. X., Cheng, M. M., Liu, S. J., Xu, J., He, Y. J., and Meng, F.: The contribution of residential coal  
692 combustion to PM<sub>2.5</sub> pollution over China's Beijing-Tianjin-Hebei region in winter, *Atmos. Environ.*, 159, 147-161,  
693 <https://doi.org/10.1016/j.atmosenv.2017.03.054>, 2017.

694 Zheng, H., Kong, S. F., Yan, Q., Wu, F. Q., Cheng, Y., Zheng, S. R., Wu, J., Yang, G. W., Zheng, M. M., Tang, L. L., Yin,  
695 Y., Chen, K., Zhao, T. L., Liu, D. T., Li, S. L., Qi, S. H., Zhao, D. L., Zhang, T., Ruan, J. J., and Huang, M. Z.: The  
696 impacts of pollution control measures on PM<sub>2.5</sub> reduction: Insights of chemical composition, source variation and health  
697 risk, *Atmos. Environ.*, 197, 103-117, <https://doi.org/10.1016/j.atmosenv.2018.10.023>, 2019.

698 Zhou, C. S., Chen, J., and Wang, S. J.: Examining the effects of socioeconomic development on fine particulate matter (PM<sub>2.</sub>  
699 <sub>5</sub>) in China's cities using spatial regression and the geographical detector technique: *Sci. Total Environ.*, 619, 436-445,  
700 <https://doi.org/10.1016/j.scitotenv.2017.11.124>, 2018.

701 Zhu, Y. J., Xie, J. G., Huang, F. M., and Cao, L. Q.: Association between short-term exposure to air pollution and COVID-  
702 19 infection: Evidence from China, *Sci. Total Environ.*, 727, <https://doi.org/10.1016/j.scitotenv.2020.138704>, 2020.

703 Zong, Z., Wang, X. P., Tian, C. G., Chen, Y. J., Qu, L., Ji, L., Zhi, G. R., Li, J., and Zhang, G.: Source apportionment of  
704 PM<sub>2.5</sub> at a regional background site in North China using PMF linked with radiocarbon analysis: insight into the  
705 contribution of biomass burning, *Atmos. Chem. Phys.*, 16, 11249-11265, <https://doi.org/10.5194/acp-16-11249-2016>,  
706 2016.

707 Zou, B. B., Huang, X. F., Zhang, B., Dai, J., Zeng, L. W., Feng, N., and He, L. Y.: Source apportionment of PM<sub>2.5</sub> pollution  
708 in an industrial city in southern China, *Atmos. Pollut. Res.*, 8, 1193-1202, <https://doi.org/10.1016/j.apr.2017.05.001>, 2017.  
709  
710  
711